



Contribution of gravity waves to shear in the extratropical lowermost stratosphere: insights from idealized baroclinic life cycle experiments.

Madhuri Umbarkar and Daniel Kunkel

Institute for Atmospheric Physics, Johannes Gutenberg University Mainz, Germany

Correspondence: Madhuri Umbarkar (mumbarka@uni-mainz.de)

Abstract. Mixing significantly influences the redistribution of trace species in the lower stratosphere, potentially being the dominant factor in forming the extratropical transition layer (ExTL). However, the role of small-scale processes contributing to mixing is poorly characterized. In the extratropics, mixing processes are often linked to stratosphere-troposphere exchange (STE), which occurs frequently during baroclinic life cycles, e.g., near tropopause folds, cut-off lows, or stratospheric streamers. Gravity waves (GWs), a dynamical feature of these life cycles, can potentially contribute to STE and mixing in the lower stratosphere. We present a series of baroclinic life cycle experiments with the ICOsahedral Non-hydrostatic (ICON) model to study the impact of GWs on the occurrence of vertical wind shear and consequent potential turbulence, an indicator for mixing in the lowermost stratosphere (LMS). Dry adiabatic simulations with varying spatial resolution reveal that the spatiotemporal occurrence of GWs depends on model grid spacing and is closely linked to shear and turbulence generation. Further process understanding is gained from experiments incorporating physical processes like latent heating, (vertical) turbulence, and cloud microphysics. Introducing moist processes amplifies GW activity and turbulence potential, mainly driven by latent heat release and stronger baroclinic wave evolution with vigorous vertical motions. Turbulence parameterization has a lesser effect on the overall evolution without moisture, while it dampens the effect of latent heat release in moist simulations. Altogether, GWs substantially enhance vertical shear and potential turbulence occurrence in the LMS and thus can play a significant role in tracer mixing and, consequently, in the ExTL formation.

1 Introduction

Atmospheric gravity waves (GWs) play a pivotal role in the dynamics of the Earth's middle atmosphere, transporting energy and momentum and hence significantly contributing to the atmospheric energy budget. GWs are mainly generated in the lower atmosphere due to various sources such as topography, jets, fronts, convection, and strong wind shear (Fritts and Alexander, 2003; Achatz et al., 2024). They propagate both vertically and horizontally with a major portion of their momentum flux carried by waves originating in the troposphere. During ascend the amplitude of these waves increases due to the decreasing atmospheric density. In turn, this amplification can lead to saturation and thus breaking of the gravity waves. In this process, GWs deposit momentum, which in turn acts as a forcing mechanism for the large-scale



25 circulation in the stratosphere and mesosphere (Andrews et al., 1987). Locally, wave breaking can cause turbulence in
 the stratosphere and mesosphere (Hodges Jr., 1967).

In recent years, there has been growing interest in understanding the contribution of small scale dynamics, specifically
 GWs to stratosphere-troposphere exchange and mixing in the upper troposphere and lower stratosphere (UTLS)(e.g.,
 30 Luderer et al., 2007; Kunkel et al., 2019; Lachnitt et al., 2023). The UTLS is an intriguing region for GW studies due to its
 characteristics of jet streams, strong inhomogeneities in wind fields, temperature gradients, as well as abrupt changes in
 atmospheric stability. These characteristics chiefly influence GW propagation and a potential source for GW dissipation.
 Moreover, this makes the UTLS both a source and a sink of GWs. Regions of baroclinic instability and jet streaks are
 often associated with enhanced GW activity, forming hotspots where GWs are frequently generated and interact with
 35 the background flow (Plougonven and Snyder, 2005). Consequently, the UTLS serves as an important source region for
 GWs, shaping their propagation and interaction with larger scale atmospheric processes.

GWs strongly influence the dynamical and thermodynamical structure of the atmosphere, particularly in the UTLS.
 By interacting with the background flow, GWs can amplify the strong vertical wind shear, from now on vertical shear,
 40 often leading to the regions of reduced static stability. Such interactions can give rise to the tropopause shear layer
 (TSL, Kaluza et al., 2021), quantified as the occurrence frequency of enhanced vertical shear, $S^2 = (\frac{\partial u}{\partial z})^2 + (\frac{\partial v}{\partial z})^2$, i.e.
 the squared vertical gradient of the horizontal wind components u and v . This pronounced strong vertical shear just
 above the tropopause in the extratropics often occurs in regions where GW activity is prevalent, such as areas of baro-
 clinic instability, jet streaks, and upper-level frontal zones (Koch et al., 2005; Wang and Zhang, 2007). Lane et al. (2004)
 45 demonstrated that GWs propagating through strongly sheared flow above the jet can generate clear air turbulence (CAT)
 driven by wave induced momentum deposition interacting with background shear. Moreover, GWs play a pivotal role in
 modulating the stability of the tropopause inversion layer (TIL), a thin layer above the tropopause characterized by a sharp
 increase in static stability (Kunkel et al., 2014). Through wave breaking, momentum deposition, and induced instabilities,
 GWs can influence the vertical structure of stability and help maintain the sharp stratification of the TIL (Zhang et al.,
 50 2015; Kunkel et al., 2019; Zhang et al., 2019). This bidirectional interaction between GWs and stability gradients plays
 a fundamental role in maintaining the TIL structure, which acts as a barrier to vertical mixing and influences large scale
 stratosphere-troposphere exchange (STE, Erler and Wirth, 2011; Zhang et al., 2015).

GWs further significantly influence tracer transport and mixing in the UTLS, particularly through the generation of tur-
 55 bulence. GWs can foster the generation of turbulent flows. One way is to enhance the strong vertical shear, which leads
 to dynamical instabilities such as Kelvin-Helmholtz instability (KHI), or another possibility is wave breaking at critical levels
 where the phase speed of waves matches the background wind (e.g., Shapiro, 1978; Whiteway et al., 2004; Lane and
 Sharman, 2006) leading to localized turbulent mixing. These processes are prominent in the extratropical transition layer
 (ExTL), a chemical tracer based transition zone around the tropopause, where turbulence facilitates tracer exchanges and



- 60 cross-isentropic mixing (e.g., Hoor et al., 2004; Pan et al., 2006). This mixing layer, where the tracer-based tropopause indicates a blurred boundary between stratospheric and tropospheric air masses (Hegglin et al., 2009), is a direct consequence of STE and turbulent diffusion. More so, the ExTL is part of the lowermost stratosphere (LMS), which can broadly be defined as the region between the height of the extratropical and tropical tropopause (Weyland et al., 2024).
- 65 Observational studies including airborne measurements and radiosonde data, show that turbulence in the ExTL enhances the vertical redistribution of chemical tracers, such as ozone and water vapor, as well as other radiatively active species, impacting UTLS composition and influencing radiative and dynamical processes (Hoor et al., 2004; Birner et al., 2002; Birner, 2006). This and the modulation of potential vorticity (PV) gradients near the tropopause suggest that GWs might play a role in enhancing mixing and modifying the structure of the mixing layer (e.g., Kunkel et al., 2019). High-
- 70 resolution numerical simulations emphasize the role of GWs in enhancing wind shear and triggering instabilities, leading to efficient mixing in the UTLS (Zhang et al., 2015; Spreitzer et al., 2019). Additionally, simulations of midlatitude cyclones reveal the impact of tropospheric jet streak, wind speed, shear enhancement, and GWs on CAT occurrence, highlighting their interaction with wind shear profiles (Trier et al., 2020; Lane et al., 2004). Evidence from the DEEPWAVE (Deep Propagating Gravity Wave Experiment) campaign has shown that orographic GWs can induce cross-isentropic mixing through
- 75 turbulence (Lachnitt et al., 2023). This mixing led to irreversible changes in tracer distributions, providing direct proof of the role of GW-induced turbulence in shaping the UTLS composition. These findings underscore the coupling between GW dynamics and mixing processes, particularly within ExTL, where chemical gradients are sharpest and small-scale dynamics play a crucial role in vertical transport and mixing, further influencing large-scale atmospheric processes.
- 80 Sources of GWs in the extratropical atmosphere can be manifold. Many GWs results from flow over topography (e.g., Durran, 1995; Lachnitt et al., 2023), while the GWs can also emerge above the convective systems (e.g., Lane et al., 2001; Fritts and Alexander, 2003; Lane and Sharman, 2006; Alexander et al., 2010). Another important source is baroclinic waves with their jet and fronts (O'sullivan and Dunkerton, 1995; Plougonven and Zhang, 2014). In the extratropical atmosphere, this source is commonly associated with baroclinic waves, but still can be regarded as a less well understood
- 85 source of GWs. Surface fronts and upper level jet streams associated with baroclinic wave development, generate GWs primarily through spontaneous imbalance, where deviations from geostrophic flow trigger wave emission (Plougonven and Zhang, 2013; Zhang et al., 2015). Particularly, these GWs are emitted along jet streaks and frontal zones propagate more horizontally and, while interacting with the background flow can foster the generation of shear and turbulence (e.g., Plougonven and Snyder, 2005; Zülicke and Peters, 2006; Trier et al., 2020; Kaluza et al., 2021). This source of GWs is
- 90 particularly significant because baroclinic life cycles which are quasi-periodic, being large-scale wave patterns in midlatitudes, are a persistent feature of extratropical atmosphere, with 4-8 distinct baroclinic waves typically evident (Hoskins et al., 1985). Ultimately, the GWs associated with baroclinic waves affect the tropopause structure and may significantly contribute to mixing in the UTLS. In particular, their contribution for shear occurrence in the UTLS has not been systematically studied despite the indications presented in recent years (e.g., Kunkel et al., 2014; Zhang et al., 2019; Kaluza et al.,



95 2021).

A way to approach baroclinic life cycles and processes within is to use an idealized numerical representation of these waves. In fact, several studies used idealized setups to study GWs within baroclinic life cycles. In a first series of experiments, O'sullivan and Dunkerton (1995) were the first to show that GWs, more precisely inertia gravity waves, emerge
 100 in dry adiabatic baroclinic life cycles in regions of the jet stream. However, they did not analyse their role for shear or turbulence generation. Wei and Zhang (2014) studied the effect of additional moisture in the setup on the appearance of the GWs. Although they show that the convectively generated GWs emerge much earlier in fast-growing moist baroclinic wave, their role in the subsequent mixing was not explored. Kunkel et al. (2014) show that GW from baroclinic waves can alter the tropopause structure and generate an environment prone to mixing and STE. However, they did not systemati-
 105 cally study the role of GWs on shear generation and the consequences for turbulence occurrence.

In this study, we utilized some ideas from previous studies to better understand the role of GWs associated with baroclinic life cycles on the generation of shear and consequent turbulence in the lowermost stratosphere. We do this in the framework of idealized baroclinic life cycle experiments of varying complexity with the ICOsahedral Non-hydrostatic
 110 (ICON) model. Specifically, we address the following questions: i) How does the ICON model resolve GWs in idealized baroclinic life cycle simulations, and where do these waves emerge relative to the tropopause location? ii) Are these GWs associated with instabilities in the lowermost stratosphere, which could lead to mixing? and iii) How much do GWs contribute to the enhanced shear in the lower stratosphere?

The paper is organised in the following manner: in section 2, we introduce the model configuration, and give an overview of the experiments used in this study. In section 3, we provide a detailed examination of the evolution of baroclinic life cycles and the spatial resolution sensitivity experiments, with the GWs appearance therein. Then, we take a closer look at some GW events. Section 4 discusses the occurrence of shear and turbulence in the LMS and their relation to the small-scale GWs in different baroclinic life cycles. We further provide a comprehensive analysis of the possible contribution of
 120 GWs in the generation of TSL in section 5. Finally, we summarize outcomes from the idealistic approach and provide some concluding remarks in section 6.

2 Model configuration and numerical experiments

2.1 Adiabatic model configuration

We conducted baroclinic life cycle (BLC) experiments in an idealized configuration of the non-hydrostatic ICON model
 125 (Zängl et al., 2015). Firstly, the dynamical core of ICON is used to simulate the dry adiabatic experiments. In this study, the ICON model is set up over the global domain, from the surface up to a height of 35 km. ICON uses the icosahedral triangular grid that provides nearly homogeneous coverage of the globe, alleviating numerical stability concerns caused



by the so-called "pole problem" on traditional latitude-longitude grids. To mitigate the reflection of upward propagating waves back into the computational domain, the sponge covers the upper 13 kilometers of the model domain. Free slip
 130 boundary conditions are applied at the surface in ICON, assuming zero tangential wind velocity, representing smooth flow over the surface without friction. The ICON model effectively simulates atmospheric dynamics by numerically solving the fully compressible, non-hydrostatic Navier-Stokes equations. The time integration of ICON combines the Matsuno scheme and the Heun scheme (also known as the trapezoidal scheme), commonly known as the predictor-corrector scheme (Zängl et al., 2015). Numerical hyper-diffusion is used to reduce the impact of inherently produced grid-scale
 135 checkerboard error patterns on numerical simulations. In the dry dynamical experiments, we exclude the topography and moisture, which eliminates the possibility of the generation of gravity waves by topography or diabatic heating. Thus, the GWs in this simulations are generated internally.

2.2 Physical parameterizations

The atmospheric physics module of ICON comprises a multitude of schemes designed to depict diabatic and turbulent
 140 processes at the subgrid-scale and their influence on the resolved circulation. In our simulations, we want to investigate the impact of certain physical processes on gravity waves. In particular, our focus is to examine the impact of latent heating and turbulence on the gravity waves and, ultimately, the emergence of shear and dynamic instability in the lowermost stratosphere. To accomplish this, we include a minimal set of physical parameterizations that reliably represent these processes. A detailed description of such diabatic processes formulation are given in Prill et al. (2020). We briefly outline
 145 the schemes used in our simulations, with further details provided in the next section.

2.2.1 Turbulence: vertical transfer and diffusion

We employ the moist turbulence scheme TURBDIFF (TURBulent DIFFusion) developed by Raschendorfer (2001), which emphasizes the distinction between turbulence and potential non-turbulent components of the subgrid-scale energy spec-
 150 trum. This distinction introduces additional scale interaction terms in the prognostic TKE equation, accounting for extra shear production of TKE driven by non-turbulent subgrid-scale flow structures. This scheme can also amplify the intensity of turbulent vertical mixing. Three-dimensional turbulent effects are neglected which is a valid approximation for simulations on the mesoscale, which means that horizontal homogeneity is assumed. Therefore, the Boussinesq ap-
 proximation is taken into account while parameterizing only vertical turbulent fluxes. Furthermore, the vertical change in specific humidity q_v and cloud water q_c , as well as the vertical shear of the horizontal wind components, have a substantial
 155 impact on the TKE budget equation. In the case of moist simulations, TURBDIFF includes processes related to saturation adjustment, which leads to latent heating and impacts the overall energy budget. Further information is provided in Raschendorfer (2001).



2.2.2 Cloud microphysics and latent heat release

In ICON, cloud microphysics parameterization uses a closed set of equations to calculate the formation and evolution of condensed water in the atmosphere. These provide the latent heating rates for the dynamics. Latent heating can occur as part of the microphysics scheme, chiefly via the saturation adjustment and the convection scheme which leads to convective precipitation. The saturation adjustment process converts any supersaturation into cloud water or ice, releasing latent heat and thus influencing atmospheric stability. Notably, the employment of saturation adjustment leads to latent heating, which impacts the overall energy budget. This excess energy significantly influences the dynamics of the atmosphere, marking a significant difference from the dry simulations where such effects are absent. The present study used a single-moment microphysics scheme (Seifert, 2008) which predicts specific humidity q_v along with the specific mass content of four hydrometeor categories such as cloud water, rainwater, cloud ice, and snow. This study solely focuses on understanding the impact of microphysics and, specifically, the associated latent heat release of the large-scale clouds on GWs, excluding the convective scheme, which would necessitate a more intricate configuration, including radiation and surface fluxes.

2.3 Model experiments

2.3.1 Initial state

For our initial state, we follow the setup proposed in the Dynamical Core Model Intercomparison Project (DCMIP2016, Ullrich et al., 2017) test case. The initial state is composed of a zonally symmetric background state, which is in thermal wind balance and a perturbation to trigger a faster baroclinic wave evolution. The background state is initiated globally, while introducing the perturbation only in the northern hemispheric UTLS. Consequently, a baroclinic wave will only emerge in the northern hemisphere within a period of about 15 days. We will thus only focus on the atmospheric state of the Northern Hemisphere.

Figure 1 shows the initial background state for zonal wind, potential temperature, potential vorticity, and specific humidity. In DCMIP, a weak, Gaussian-shaped wind perturbation is introduced at the center of the model domain, which points to the location (20° E, 40° N) at the altitude of the tropopause. The mid-latitude jets at 45° N/S are centered slightly below the tropopause, with the horizontal mean surface temperature of $T = 288$ K. Moreover, the zonal wind is derived under the thermal wind balance. A moist variant of the dry dynamical test is considered here to understand the impact of moisture feedback on the development of the wave. The moisture field is only initially available for simulations including moisture. We note here that we conducted all simulations discussed in the manuscript for a third initial state, following Jablonowski and Williamson (2006). The DCMIP "wind" and the Jablonowski test case have strong similarities, both leading to a life cycle that resembles the life cycle type 1 (Thorncroft et al., 1993, LC1,) while the DCMIP "stream" instead shows a life cycle development of type 2 (LC2).

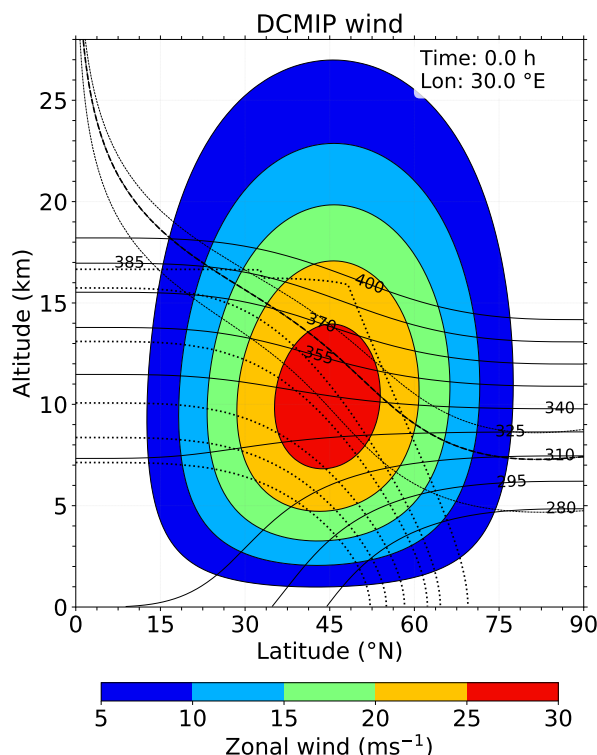


Figure 1. Zonally symmetric balanced initial conditions at 30° E longitude: zonal wind ' u ' (shaded contours, 5 ms⁻¹ spacing), potential temperature ' θ ' (solid black lines, 15 K spacing, starting with 380 K in the lower right corner) and specific humidity q_v for values 0.002, 0.02, 0.05, 0.2, 0.5, 1. g.kg⁻¹ (dotted lines, from bottom to top), the thick dashed line marks the location of dynamical tropopause, defined as the 3.5 pvu potential vorticity isosurface.

190 We will discuss both cases in our result sections since the two solutions provide some coverage of the life cycles observed in the real atmosphere. The DCMIP case with the zonal wind perturbation leads to a life cycle resembling a case known as life cycle type 1 (LC1 Thorncroft et al., 1993). This type shows the development of a stratospheric streamer along with anti-cyclonic wave breaking. The DCMIP stream function case leads to a different evolution, which has some resemblance to the life cycle type 2 described in Thorncroft et al. (1993).

195 2.3.2 Dry and moist baroclinic life cycle experiments

In total, we will discuss the results from 20 different baroclinic life cycle experiments (see Table 1). The life cycles vary in their initial state, the model resolution, or through the addition of physical processes. We conducted ten simulations with a dry adiabatic setup, five each for the two initial states, *wind* and *stream* (see table 1). In these simulations, we varied the underlying horizontal grid from 13 km (R03B07; ICON grid) to 80 km (R02B05). We changed the number of vertical levels between 40 and 100 while keeping the domain height constant at 35 km altitude. These levels resulted in



Table 1. Summary of idealized DCMIP experiments performed using ICON

*Moist: only saturation adjustment, CMP: saturation adjustment + bulk microphysics scheme

Dry adiabatic simulations		
Experiments	Short Description ICON grid	$\Delta x (\approx \text{in km}), \Delta z (\text{model levels})$
REF _{wind}	wind perturbation with R02B07	20, 100 (~ 300 m)
REF _{stream}	stream perturbation with R02B07	20, 100
HRES _{stream}	stream perturbation with R03B07	20, 100
HRES _{wind}	wind perturbation with R03B07	20, 100
MRES _{wind}	wind perturbation with R02B06	40, 100
MRES _{stream}	stream perturbation with R02B06	40, 100
MRES40 _{wind}	wind perturbation with R02B06 on 40 levels	40, 40 (~ 900 m)
MRES40 _{stream}	stream perturbation with R02B06 on 40 levels	40, 40
LRES _{wind}	wind perturbation with R02B05 on 40 levels	80, 40
LRES _{stream}	stream perturbation with R02B05 on 40 levels	80, 40
Simulations with physical forcing		
Experiments	Short description	Schemes used
REF _{wind} Moist	Wind perturbation with moisture	saturation adjustment
REF _{wind} TURB	Wind perturbation, turbulence	Raschendofer
REF _{wind} CMP	stream perturbation, cloud microphysics	single moment
REF _{wind} TURB CMP	stream perturbation, turbulence and cloud microphysics	Raschendofer + single moment
REF _{wind} TURB Moist	turbulence with moisture	Raschendofer
REF _{stream} Moist	stream perturbation with moisture	saturation adjustment
REF _{stream} TURB	stream perturbation, turbulence	Raschendofer
REF _{stream} CMP	stream perturbation, cloud microphysics	single moment
REF _{stream} TURB CMP	stream perturbation, turbulence and cloud microphysics	Raschendofer + single moment
REF _{stream} TURB Moist	turbulence with moisture	Raschendofer



roughly 900 m or 300 m grid spacing in the UTLS. The simulations with 20 km horizontal grid spacing and 100 vertical levels will be regarded as our reference simulation (REF), for which we also conducted the majority of the physics-added simulations. The other simulations are either denoted as high (HRES), medium (MRES), or low (LRES) simulations. This setup strategy allows us to study the emergence of gravity waves, shear, and potential turbulent regions in our simulations.

205 In the next step, we perform sensitivity experiments focusing on non-conservative processes, including either turbulence (further denoted as TURB) or cloud microphysics (CMP). For both initial states, we study the effect of moisture and, particularly, the effect of latent heat release on the GW, shear, and turbulence appearance. Two simulations only used the saturation adjustment scheme of the model to mainly study this latent heat feedback (MOIST). Additionally, we run two more simulations with a simple cloud microphysics scheme to address potential additional effects (CMP). We note here
 210 that the MOIST simulations have been carried out for all resolutions used in the dry adiabatic setup. However, since the general difference between dry and moist simulations is very similar, independent of the resolution, only the results for the REF cases are shown and discussed further.

We also wanted to determine whether the turbulence parameterization affects the appearance of GWs, shear, and turbulence in our simulations. For this, we run two REF simulations with the turbulence parameterization turned on
 215 (TURB). Finally, we run four REF simulations with combinations of *wind*, *stream*, TURB, MOIST, and CMP to address the combined effects of these parameterizations and initial states. More details about the simulations are given in Table 1.

3 The DCMIP baroclinic life cycle and the occurrence of gravity waves

3.1 Baroclinic evolution and gravity wave appearance in the reference simulations

We start this section with a brief introduction of the main features of the baroclinic life cycle. First, we show the evolution of
 220 the baroclinic wave using isentropic potential vorticity for the two reference simulations. We then discuss the occurrence of gravity waves that emerge during the various stages of life cycles.

Figure 2 provides an overview of the synoptic evolution of the baroclinic wave for two dry adiabatic reference simulations between 240 h and 312 h after the model starts. As will be shown later, this is the time period most interesting for our GW, shear, and turbulence analysis. The REF_{wind} and REF_{stream} simulation features the same general characteristics of the
 225 life cycle as described in Ullrich et al. (2014) and covers initial growth and rapid development of the baroclinic disturbance. Note the black line in the panels of figure 2 which highlights the 3.5 pvu isoline ($1 \text{ pvu} = 1 \times 10^{-6} \text{ Km}^2 \text{ kg}^{-1} \text{ s}^{-1}$) and marks the dynamical tropopause in our simulations Hoerling et al. (1991); Erler and Wirth (2011). Our life cycle evolves rather slowly, with the first signs of a substantially growing wave after 192 h. We consider this beneficial for two reasons: first, we can regard our results more conservatively since a slow evolution correlates with less GW emission; second, we think
 230 that numerical, spurious features occur less with a slower evolution.

As the time series highlights, both waves grow to substantial amplitudes, showing tropospheric and stratospheric intrusions, a PV streamer, and secondary cyclogenesis. They differ in the size of the PV streamer and the strength of the

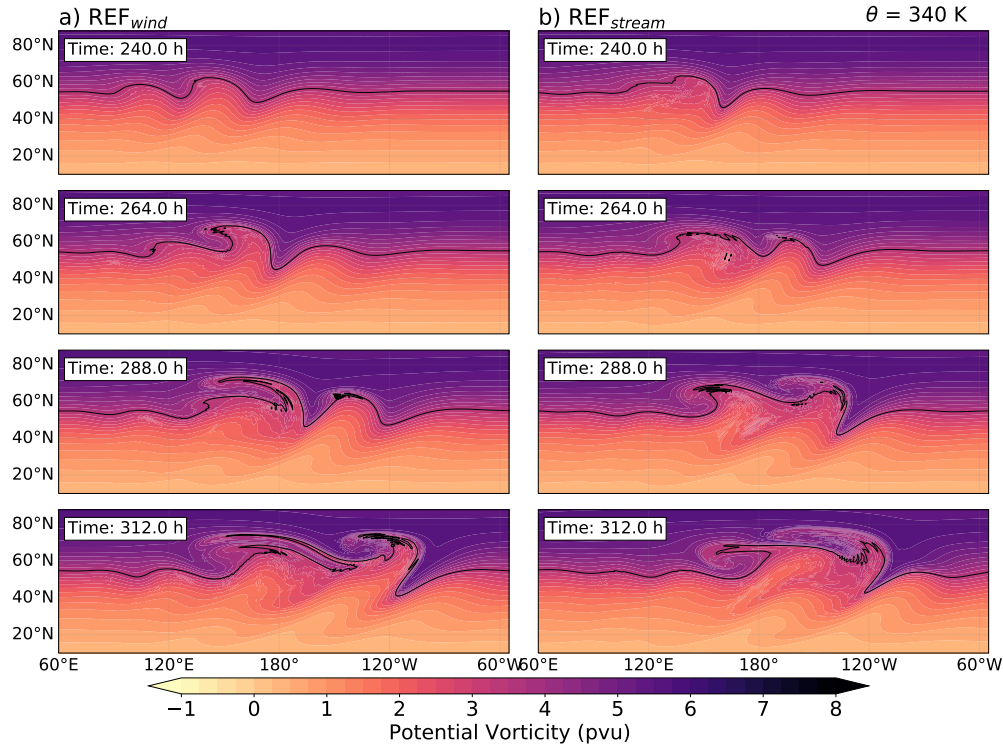


Figure 2. The evolution of the baroclinic life cycle for the a) REF_{wind} and b) REF_{stream} simulation. Horizontal cross sections of potential vorticity at 340 K isentropic surface over the Northern Hemisphere after 240, 264, 288 and 312 h of model integration. The solid black line represents the 3.5 pvu, regarded as a dynamical tropopause.

tropospheric and stratospheric intrusions. Both life cycles exhibit wave breaking. Despite their dry adiabatic nature, there are signs of PV non-conservation in the region of the steep PV gradients, potentially associated with numerical mixing.

235 Figure 3 shows the divergence of the horizontal wind components and illustrates regions where gravity waves are present in two dry adiabatic reference simulations at various time steps at an altitude of 11-km. This altitude is close to the altitude of the jet stream core (see Figure 1), thus representing well the situation of the tropopause region along the lowermost stratosphere and is taken as a representative height for further discussion. As evident in Figure 3, alternating signals in the horizontal divergence mark the presence of gravity waves in both reference simulations from 240 h onward.

240 Before, we noticed little presence of this wave, and after this time, the horizontal divergence highlights the growth of these features. The GWs have their source of imbalances in the synoptic flow and propagate into the UTLS during life cycles. The wavelength of this wave mode can be deduced from the peaks in the divergent field. In many cases, the horizontal wavelength is on the order of a hundred kilometers which is similar to wavelengths of inertia gravity waves.

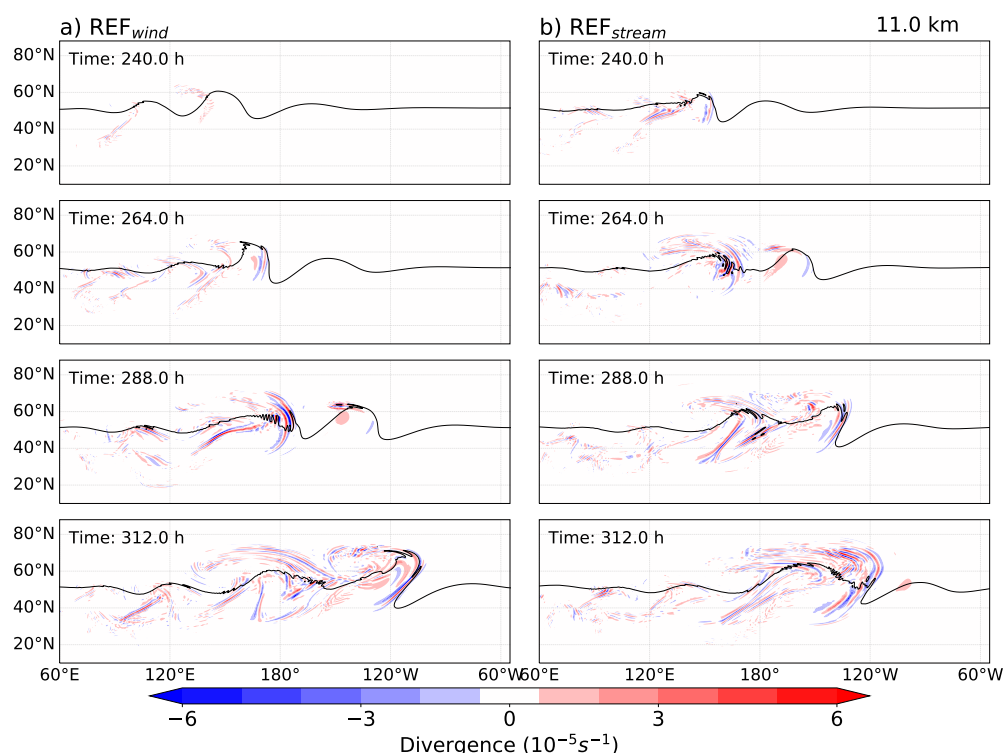


Figure 3. The evolution of the GW for the a) REF_{wind} and b) REF_{stream} simulation. Horizontal cross sections of horizontal divergence at 11-km altitude over the Northern Hemisphere after 240 h, 264 h, 288 h, 312 h of model integration, respectively. The solid black line represents the dynamical tropopause.

245 A prominent sign of a GW emerges first after 240 h in the REF_{wind} simulation around 140° E. At 264 h, this feature is evident on the tropospheric side of the jet in the ridge around 170° E. Interestingly, the wave crosses the tropopause into the lowermost stratosphere (after 288 h) and spreads out in the stratosphere over the course of the next 24 h. The GW signatures are typically observed in the jet exit region and over the northwards reaching ridges of the baroclinic wave, especially in regions characterized by pronounced PV gradients with larger amplitudes (Plougonven and Snyder, 2005; 250 Plougonven and Zhang, 2013). The jet stream in the UTLS partially excites the waves, indicating that both the surface front and the upper tropospheric jet-front system contribute as sources of these small-scale waves. This indicates that the background flow significantly influences the wave characteristics during their propagation. The larger spectrum of GWs was observed after 312 h when the baroclinic wave undergoes breaking. The wave characteristics adhere to the phases of baroclinic wave development. This aligns well with the fact that the growth rate of flow imbalance correlates with 255 the growth rate of baroclinic waves, which, in turn, strongly correlates with the frequency of GWs (Wang and Zhang, 2007).

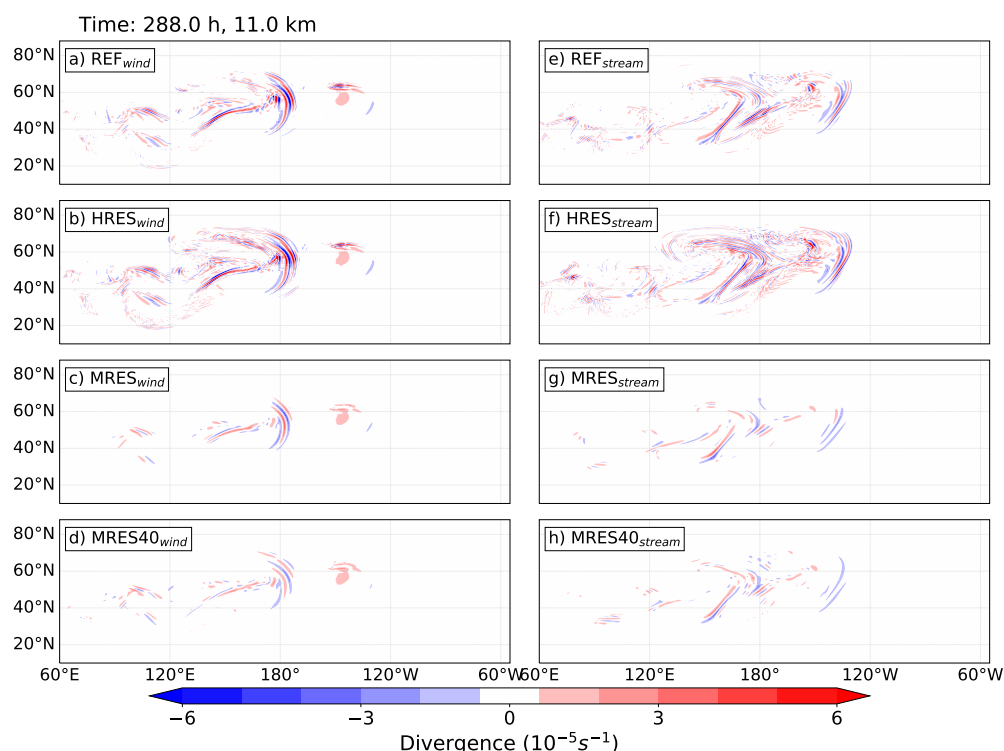


Figure 4. Evolution of gravity waves (GWs) for simulations with varying grid spacings. Panels (a-d) represent simulations with wind perturbations for experiments REF, HRES, MRES, and MRES40, respectively, while panels (e-f) show simulations with stream perturbations for the same configurations. The figure displays the distribution of the 11-km divergence of the horizontal wind field over the Northern Hemisphere after 288 h of model integration.

REF_{stream} experiment (Figure 3 right) reveals comparable temporal evolution of GWs but with slight variations in the location of GW development. The prominent signatures and the sort of curl-up feature were noticed one day prior to the REF_{wind}, resulting in the earlier appearance of GW modes. Three strong GW packets appear after 288 h, moving poleward and towards the west. The remarkable feature here is that the wave modes develop clockwise, representing the clockwise evolution of baroclinic waves. After 312 h, the REF_{stream} BLC undergoes cyclonic breaking in the lowermost stratosphere. Overall, this cyclonic wave breaking of baroclinic instability with stream perturbation resembles an LC2 type life cycle (Thorncroft et al., 1993). Even though the baroclinic wave in this form evolves quite swiftly, the wave breaking occurs later than in REF_{wind}. During the intensifying stage of BLC, features like substantial stratospheric intrusion and tropospheric wrap-up, along with the PV streamers in the horizontal divergence field, hint towards the potential turbulence in the lower stratosphere and could lead to STE.



3.2 Gravity wave occurrence: impact of horizontal and vertical grid spacing

In this section, we aim to answer how GWs emerge in low and high-resolution simulations and how the occurrence, location, and properties of GWs are influenced by the horizontal and vertical grid spacing in the upper troposphere and lower stratosphere.

In the first step, we aim to assess the resolution dependence for which we use all of our dry adiabatic simulations with differing spatial resolutions. In general, we see a similar evolution of the baroclinic wave in the different dry simulations. The main differences are evident on the mesoscale, and minor differences in the exact location of the trough. These observations are independent of the perturbation function. Since the baroclinic wave evolve quite consistently in the various simulations, there are also common regions of GW occurrence in all the simulations. The distribution of horizontal divergence at 11-km after 288 h for the aforementioned simulations is illustrated in Figure 4. In the wind perturbation simulations, this is the region of the baroclinic wave ridge (see around 180° E after 288 h at 11-km) and above the trailing surface cold front. Other hotspots for GWs are evident, particularly upstream of the jet core, where the baroclinic wave induces strong vertical motion, and downstream near the tropopause, where GWs propagate along the sharp PV gradient of the streamer. Similar regions can be identified in the simulations with the stream function perturbation.

Besides these similarities, there are notable differences which can, of course, be expected. We noticed minimal differences in GW representation when varying vertical resolution between 40 and 100 levels, with 100 levels adequately capturing the GW spectrum and their key features. The higher the model resolution, the more of the gravity wave spectrum is resolved, compare e.g., the divergence field between REF, MRES, and LRES simulations. An example of wind perturbation is the region north to surface cold front with more GW signals in the high-resolution simulations, which is virtually absent in coarser resolution viz. LRES_{stream} (not shown). Henceforth, we exclude the LRES simulations as they did not exhibit significant indications of gravity waves. A second notable difference is the amplitude of the divergent signal, which is larger in the high-resolution cases, aligning with previous findings that high resolution better captures GWs signals and their propagation (Zhang, 2004; Plougonven and Snyder, 2005). There is minor sensitivity of medium-scale waves to enhanced horizontal resolution, implying that they are being adequately resolved in REF and HRES simulations. These results support earlier studies showing that increased resolution enhances the ability to capture fine-scale GW structure and dynamics while medium scale remains relatively insensitive (Plougonven et al., 2003; Kunkel et al., 2016).

3.3 Gravity wave occurrence: impact of non-conservative processes

In this section, we explore the impact of physical processes on the evolution of the baroclinic waves and the occurrence of GWs. For this, we compare the reference simulations with simulations including latent heat feedback, i.e., Moist, a parameterization for cloud microphysics, i.e., CMP, a parameterization for turbulence, i.e. TURB, a combination of the parameterizations for cloud microphysics and turbulence, i.e., TURB CMP, and turbulence parameterization with moisture,



i.e., TURB Moist.

300

The experiments investigate the influence of moisture on GW patterns within baroclinic waves, using both wind and stream perturbations. Figure 5 shows the 11-km horizontal divergence distribution at 264 h, highlighting the evolution of baroclinic waves and showcasing various GW modes during different stages of wave development. Specifically, Figure 5a) captures the baroclinic structures in the REF_{wind} experiment, corresponding to the conditions in Figure 5b) REF_{stream}. Moist cases 5b-h) indicate noisy divergence, inconsistent with the patterns observed in REF experiments. The Moist simulation shows that wave growth begins earlier than in the dry case, likely due to the release of latent heat being an additional energy source from moisture. Noticeable differences in the divergence pattern appear across the Moist runs at this stage despite the initial moisture content being similar. The emergence of wave-like features before the appearance of the main GW pattern suggests spontaneous emission influenced by moisture. As a result, significant GWs are detected near large-scale structures. In conditions with moisture and saturation adjustment, the introduction of weak convective instability allows dry dynamic GW modes to prevail. Nonetheless, small-scale features indicative of synoptic-scale GWs in the LS reveal consistent GW activity throughout the evolution of moist baroclinic wave, which may warrant further analysis. Overall, the development of simulated moist baroclinic waves is qualitatively similar to the life cycles described by Zhang (2004) and Zhang et al. (2015). However, isolating small-scale features from the large-scale dynamics in moist scenarios remains challenging, requiring additional steps to understand their impact on mixing.

We now move our discussion to assess the impact of bulk microphysics and turbulence parameterization on the development and characteristics of GWs. These experiments are conducted using the same spatial resolution as in the REF experiment. In the TURB simulations (Figure 5c-i), the GW signature appears weaker, which could be due to the tendency of turbulence to reduce strong vertical gradients. Although turbulence acts against the effects of dry dynamics, the GW features observed in TURB are similar to the REF experiment. In the CMP experiment (Figure 5d-j), similar divergence patterns as Moist are observed around 180° W/E, explaining that the latent heat release drives these patterns. The GW patterns in the LMS indicate that moisture inclusion leads to stronger updrafts, accelerating the evolution of the GW life cycle. Processes originating from lower tropospheric levels significantly influence GW activity, and similar effects are noted in experiments with saturation adjustment, i.e., Moist, confirming that latent heat release, rather than microphysical processes, is responsible for the observed effect. Figures 5e-k) and 5f-l) display the TURB CMP and TURB Moist cases, respectively, for both initial states. After 264 h of model integration, similar structures of GWs are observed in these experiments, with minor variations in GW characteristics. Specifically, GWs are more prominent in the TURB Moist case, while the TURB CMP shows differences in GW locations, with more subsequent waves emerging. The TURB CMP closely resembles the REF_{wind} CMP, suggesting that microphysical processes play a more dominant role than turbulence. Overall, distinct variations in GW patterns across all physics experiments are evident at this stage of the life cycle.

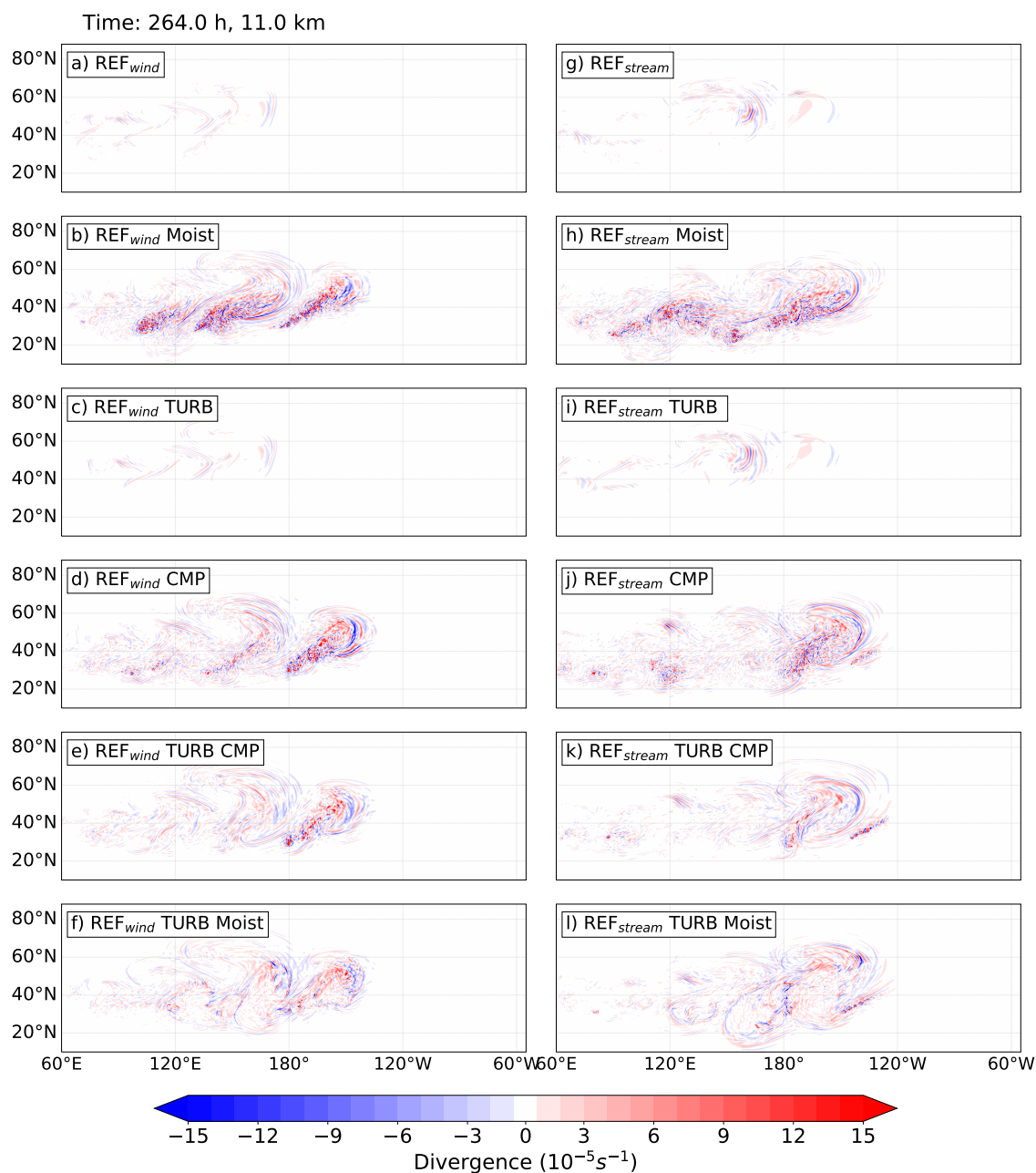


Figure 5. As in Figure 4 but after 264 h for the simulations with varying physical processes. Top panel a)-b) represents the corresponding reference simulations.

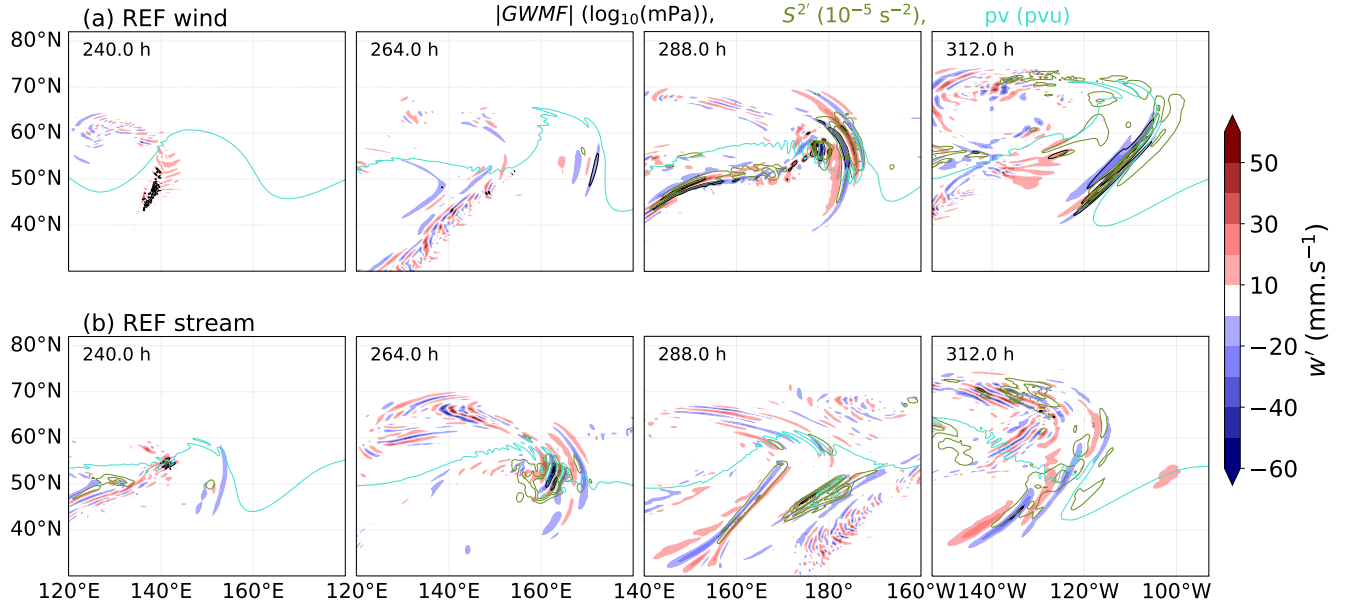


Figure 6. Horizontal evolution of 11-km perturbation vertical velocity w' in mm.s^{-1} from 240 h to 312 h of model integration for REF_{wind} and $\text{REF}_{\text{stream}}$ experiment. The absolute GW momentum flux $|GWMF|$ in $\log_{10}(\text{mPa})$ (black), vertical wind shear $S^{2'}$ in 10^{-5} s^{-2} (green) from the spectral domain. The turquoise lines denote the 11-km dynamical tropopause where potential vorticity equals 3.5 pvu.

Taken together, in all Moist physics experiments, latent heat release, a consequence of condensation, enhances vertical motions in the tropospheric region, which extend to the UTLS, creating a vertical gradient barrier. The air parcel
 335 above is already in the sinking motion, exhibiting enhanced upward motions. The processes in Moist experiments differ fundamentally from those in dry scenarios, leading to significant variations in GW emergence in the lower stratosphere. The rapid, small-scale lifting processes associated with these upward motions drive the faster evolution of the GW life cycle, resulting in earlier wave breaking compared to the dry case. This demonstrates that incorporating moisture in the model accelerates GW evolution due to the enhanced upward motions caused by latent heat release throughout the life
 340 cycle. Nevertheless, the physical processes leading to GW occurrence seem to be similar in LC1 and LC2.

3.4 Gravity wave occurrence: connection with vertical shear

Our primary goal is to analyze the connection between GW occurrence in baroclinic life cycles and their potential to contribute to the formation of the shear layer above the tropopause and potential mixing. So far, we have shown that GWs emerge over varying setups regarding the initial state, the grid spacing, and the complexity in light of process
 345 representation. Before we dive deeper into the analysis of shear and turbulence in these simulations, we want to briefly highlight the spatial and temporal connection between the occurrence of GWs and enhanced vertical shear. For this, we



again focus on the dry reference simulations.

Figure 6 shows the temporal evolution of GW packages reconstructed from the spectral domains at 11-km altitude for REF_{wind} and REF_{stream}. The location of the GWs is analyzed via two metrics: the vertical wind perturbations w' and the absolute momentum flux. This is a momentum flux of the sub-synoptic scales, which we refer to as a first proxy for the momentum flux due to GWs (GWMF). We use w' instead of divergence because both are interconnected, and w' is directly linked to the GWMF. w' as all other prime quantities here represent filter quantities. The filter is applied in spectral space and removes the contributions from wavenumber 0 to 8. The GWMF is then computed as follows:

$$|\text{GWMF}| = \rho \sqrt{(u'w')^2 + (v'w')^2}$$

where ρ_0 is the mean density, u' , v' and w' are the zonal, meridional and vertical velocity perturbations, respectively. Additionally, the panels show the vertical shear for the small scales estimated as $S^{2'} = \left(\frac{\partial u'}{\partial z}\right)^2 + \left(\frac{\partial v'}{\partial z}\right)^2$. Velocity perturbations initially emerge above the low-level trough with small magnitudes, which then gradually intensify and form the organized wave structure in the eastern trough. These GW packets are identified by their horizontal wavelength (~ 100 km). We find the regions of divergence-convergence of vertical velocity in LS, which often results from emerging GWs from the updrafts but is also present in the regions of eastward propagating GWs. More so, an increase in vertical shear is observed near GWs above lifted air masses reaching tropopause. The shear location relative to the phase of low-level baroclinic waves remains consistent with GWs throughout the simulation. Notably, maxima of $S^{2'}$ occur above the tropopause, overlapping significantly with the regions of peak GWMF. This alignment implies a potential interaction between GWs and shear, suggesting that energy/momentum transfer due to GWs may contribute to and/or be influenced by the vertical shear in the LS. The remarkable overlap of GW and shear occurrence motivates a deeper look at the link between these two features and ultimately on potential turbulence occurrence.

4 Shear and turbulence diagnostics in the LMS

4.1 Vertical shear

In the following, our discussion centers on investigating the role of GW in the generating shear, which could lead to turbulence in the LMS. On sub-synoptic scales, GWs are well known to influence the temperature and wind field in the lower stratosphere, which consequently affects the static stability and the vertical shear of the horizontal wind (Kunkel et al., 2014; Kaluza et al., 2019). Thus, GW plays a role in the formation of the tropopause inversion layer (Birner, 2006; Kunkel et al., 2014; Zhang et al., 2019) and may also play a role in the tropopause shear layer (Kaluza et al., 2021). We focus our analysis and discussion on the occurrence of strong wind shear, in line with this on static stability N^2 . Ultimately, we focus our discussion on the occurrence of dynamic instability and potential turbulence due to GW-induced shear in the LMS.

Instabilities are a key prerequisite for mixing of air parcels in the atmosphere. This section focuses on shear-driven instabilities such as Kelvin Helmholtz instability (KHI), which can be diagnosed through the gradient Richardson number,

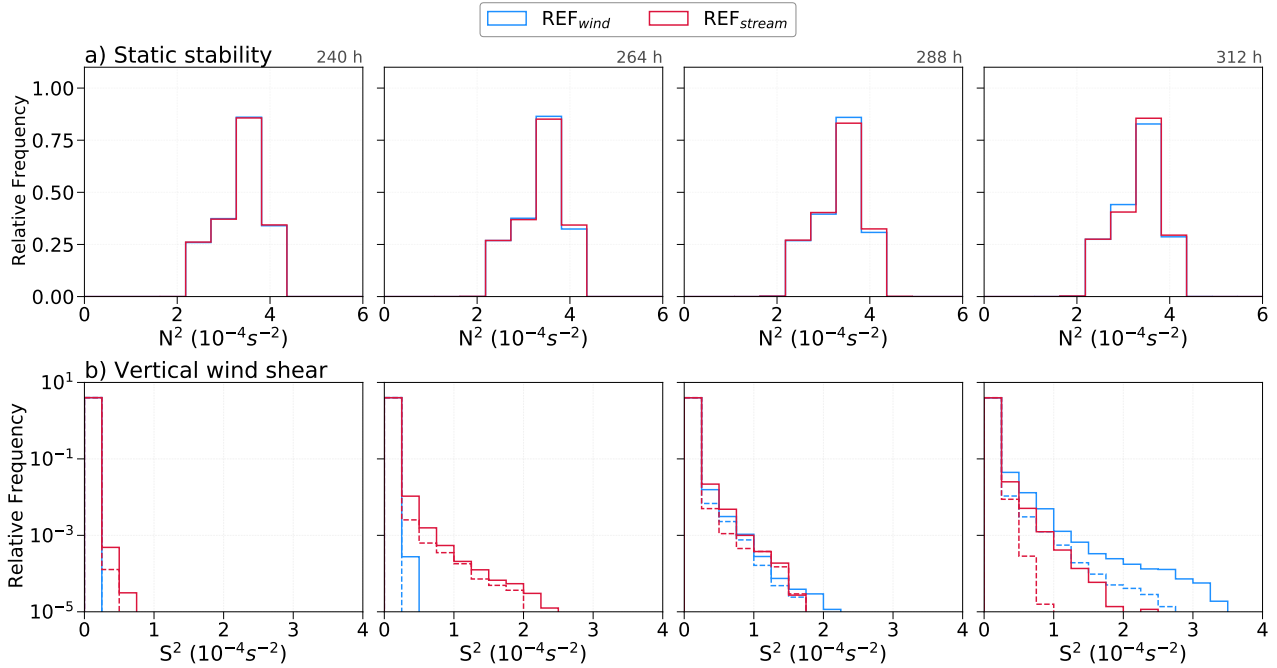


Figure 7. The temporal evolution of PDFs of a) static stability, N^2 and b) vertical wind shear, S^2 in the lowermost stratosphere for dry reference experiments. The dashed histograms in b) represents $S^{2'}$ from spectral domain for the respective REF simulations.

Ri. Moreover, according to linear wave theory, the dynamic instability of the flow can be evaluated based on the non-dimensional Richardson number $Ri = \frac{N^2}{S^2}$, which can be defined as the ratio between static stability and the vertical shear of the horizontal wind. In contrast to the static or convective instability, diagnosed via negative squared Brunt-Väisälä frequency, N^2 , KHI is a hydrodynamic or dynamic instability, which requires a weaker criterion to be fulfilled for the flow to become unstable. Theoretical considerations require that Ri falls below a critical Richardson number, which is set to $Ri_c = 1/4$. However, in studies using output from numerical models on the resolution used in this study, a larger value is often used to identify regions prone to dynamic instabilities (e.g., Kunkel et al., 2019; Kaluza et al., 2022). We also regard regions of low Richardson numbers, i.e., $Ri \leq 5$, as being prone to turbulent mixing.

In our analysis of shear and turbulence, we initially focus on the lowermost stratosphere (LMS), defined here as the region between the dynamical tropopause, i.e., 3.5 pvu and the 380 K isentropic level, which corresponds to the maximum potential temperature of the tropical lapse rate tropopause (e.g., Holton et al., 1995; Shepherd, 2007). This is the region in the extratropics where the mixing layer resides. We start our analysis with probability density functions (PDFs) of N^2 , S^2 and $S^{2'}$ in the LMS and focus on the time with significant GW activity, i.e., from 240 h onward in the dry reference simulations (see Figure 7). Here, two important implications become evident. First, the distribution of static stability is relatively constant with time and perturbation method (Figure 7a). Second, the distribution of S^2 in Figure 7b shows

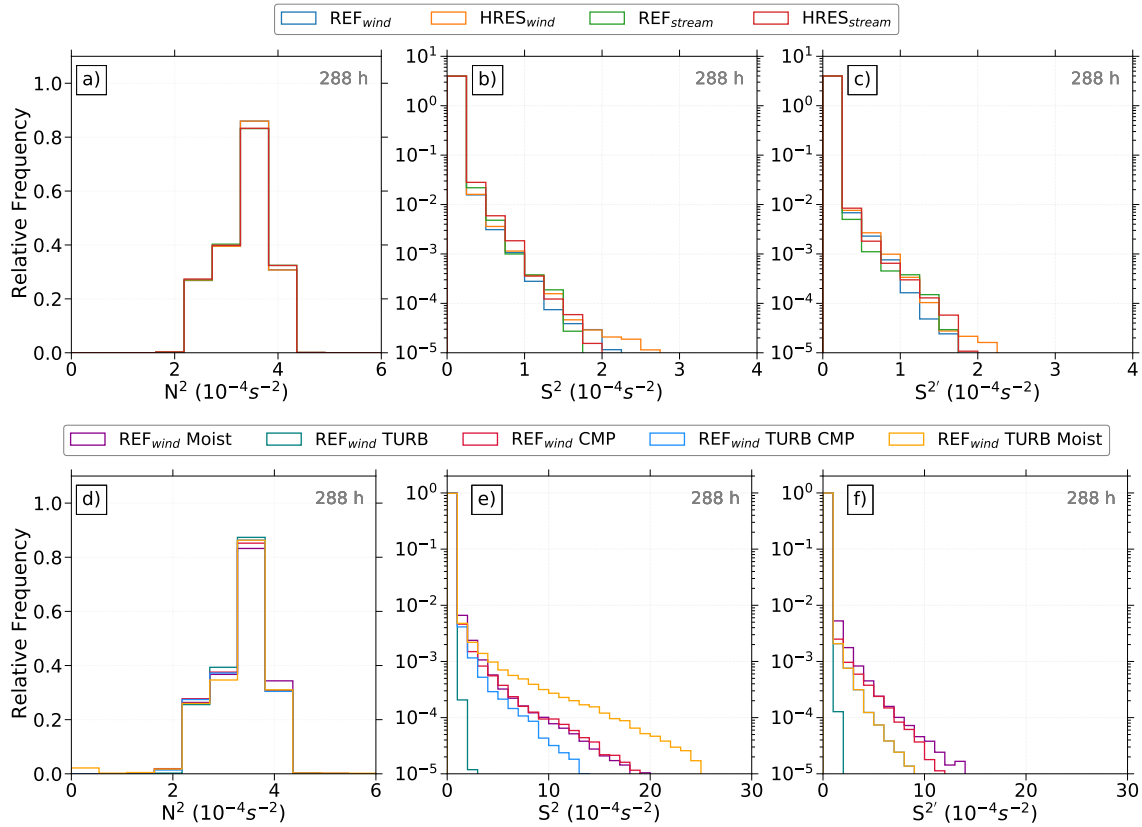


Figure 8. Temporal evolution of relative occurrence frequency distribution of N^2 (a-d), S^2 (b-e) and $S^{2'}$ (c-f) in the lowermost stratosphere over the northern hemisphere. Upper panel (a-b-c) represents grid spacing sensitivity experiments. Lower panel (d-e-f) represents physics sensitivity experiments performed using wind perturbation function. LMS is defined as the region between 3.5 pvu, a dynamical tropopause and 380 K isentropic surface.

395 variations with time on the right side of the distribution whereas $S^{2'}$ majorly follows the trend of S^2 . There is an increase in the occurrence of larger S^2 values with time. Although the changes in S^2 PDFs differ between the two perturbation methods, both exhibit a similar overall behavior. Notably, the increase in S^2 and particularly $S^{2'}$ is temporally aligned with the occurrence of GWs in the simulations. Under the assumption that $S^{2'}$ is strongly under the influence of GW activity, this, in turn, suggests a substantial contribution of GW to the generation of the largest shear values. This also reveals that
 400 the major part of total S^2 in the LMS resembles the small-scale shear.

An analysis of N^2 and S^2 - $S^{2'}$ PDFs for our sensitivity experiments with respect to grid spacing and physical forcing further suggests that GW may play a dominant role in the generation of the largest shear values. While the distributions of static stability in the LMS show comparable distributions among the sensitivity simulations, notable differences between
 405 the simulations arise for vertical shear (see Figure 8). These differences can be summarized as follows: the finer grid

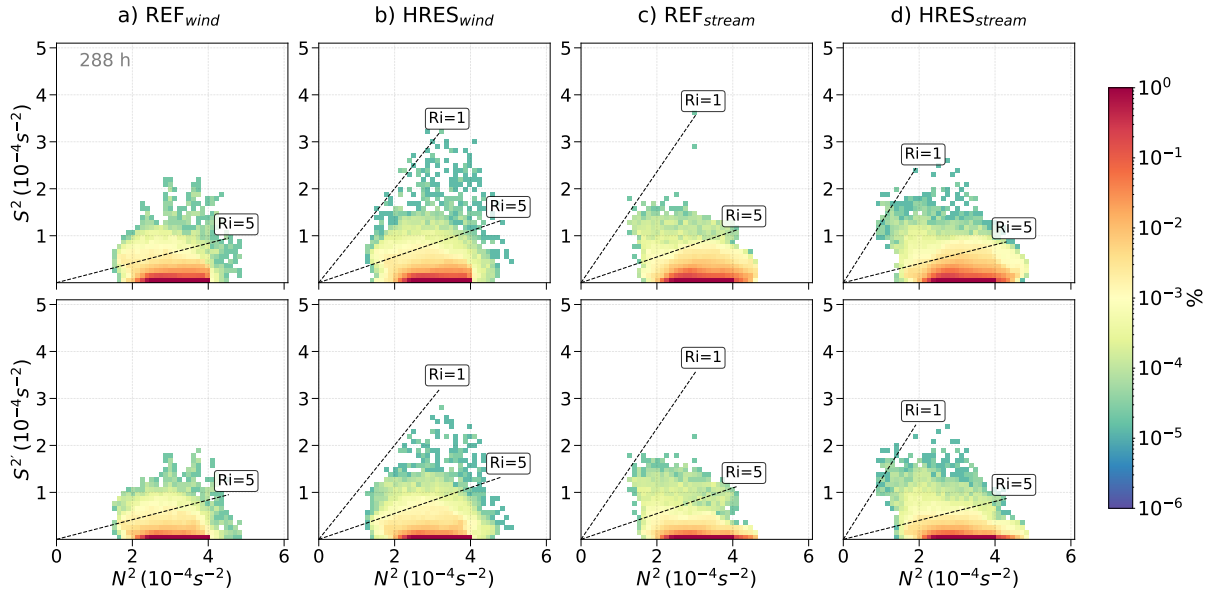


Figure 9. Relative occurrence frequency distribution of N^2 - S^2 (upper panel) and N^2 - $S^{2'}$ (lower panel) pairs after 288 h for simulations with varying grid sensitivity over northern hemisphere in the lowermost stratosphere. Logarithmic occurrence frequency color scale. Dashed lines indicates the gradient Richardson numbers.

spacing leads to more enhanced shear values, while moist dynamical processes drastically enhance the maximum shear values. However, the very strong S^2 observed in TURB Moist results in relatively fewer $S^{2'}$ occurrences in the spectral domain, likely due to enhanced turbulence indicated by turbulent kinetic energy (TKE), which suppresses small-scale variability in shear. These findings align with our observations of GW appearance, further supporting the hypothesis that
 410 GWs play a key role in generating the largest shear values in the LMS in our baroclinic life cycle experiments.

4.2 Dynamic instability and turbulence

On smaller scales and in instantaneous considerations, we observed significant general co-location of enhanced GW activity and enhanced S^2 and $S^{2'}$ occurrences in the LMS. Now we move our discussion to the potential occurrence of turbulence in the LMS and additionally discuss the relation between N^2 , S^2 , $S^{2'}$ and Ri using a two-dimensional density
 415 function (compare their Figure 14a Kaluza et al., 2021). Turbulence is a rare event, even in the LMS, and is even rarer than enhanced vertical shear. As such, only a few data points are expected to exhibit small-scale turbulence. This becomes evident when using two-dimensional probability density distributions with the axes being the squared Brunt-Vaisälä frequency N^2 and the vertical shear of the horizontal wind (i.e., S^2 or $S^{2'}$). The color shows the relative frequency of N^2 and S^2 values in the LMS with respect to Ri (Figure 9). We also added black dashed lines to mark values for the gradient
 420 Richardson number. For $Ri \leq 5$, the potential for the occurrence of a dynamic instability is given. Note that only data points in the LMS are considered for this analysis. Thus, we only see turbulence and enhanced shear occurrence above

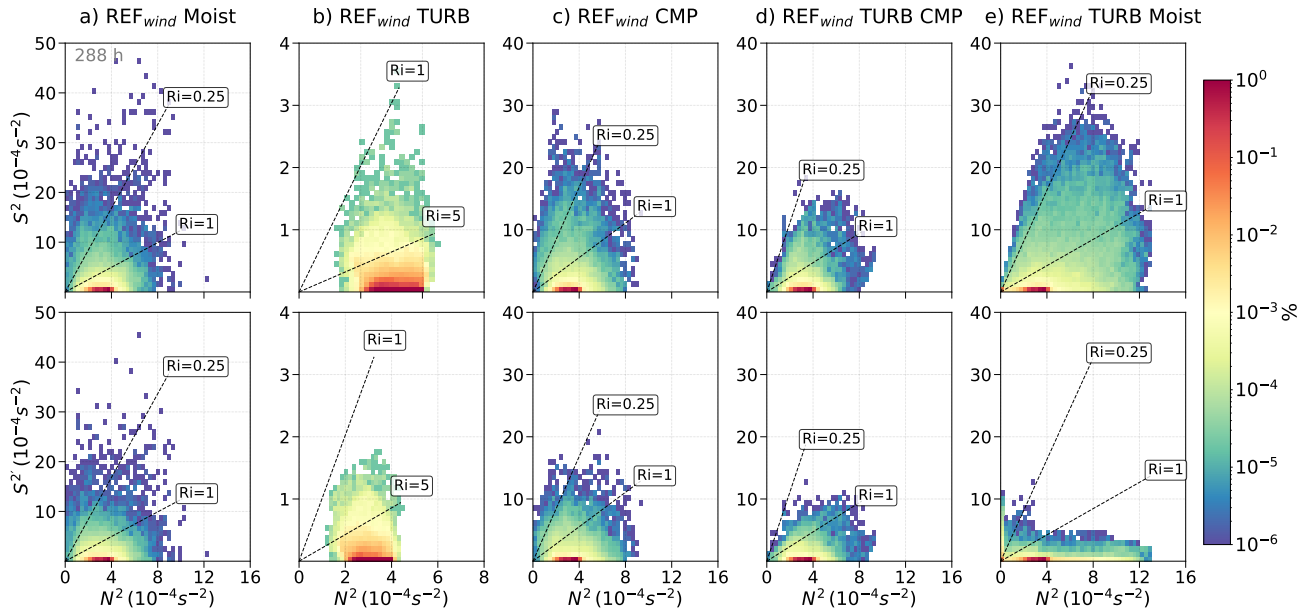


Figure 10. As in Figure 9 but after 288 h for the REF_{wind} simulations with varying physical processes.

the the local 3.5 pvu tropopause and below 380 K. We also note that we focus on individual time steps and compare the PDFs for various simulations, which again helps to highlight the differences between the simulations.

425 We start again with the dry adiabatic reference experiments and their high-resolution companions (REF and HRES, see Figure 9). The results show that turbulence and enhanced shear are rare events with few grid volumes falling below $Ri \leq 1$. For wind perturbations, HRES produces more regions of enhanced S^2 and tends to exhibit slightly more turbulence-prone areas compared to REF simulation, highlighting the stronger influence of higher resolution in capturing these features. In contrast, stream perturbations show greater similarity between HRES and REF, with only marginally
 430 enhanced shear and turbulence occurrences in HRES. Overall, S^2 and $S^{2'}$ show only weak differences, especially for larger values, indicating that smaller scales contribute substantially to the shear occurrence. HRES captures finer details and shows slightly more enhanced shear and turbulence than REF, as expected, with smaller scales contributing significantly to these enhanced values. The dynamically stable LMS persists throughout most of the simulation, with a brief indication of potential turbulence during wave breaking. This indicates that the dry experiments exhibit evidence of
 435 potential dynamical instability in the LMS, with GWs as a potential contributor to turbulence generation.

Figure 10 continues to demonstrate the temporal evolution of N^2 - S^2 pairs with Ri in sensitivity experiments with physical processes. The observed latent heating, i.e., REF_{wind} Moist (Figure 10a), is shown to increase the occurrence of enhanced shear in the LMS. The N^2 - S^2 and N^2 - $S^{2'}$ pairs show in all cases with moisture that Richardson numbers

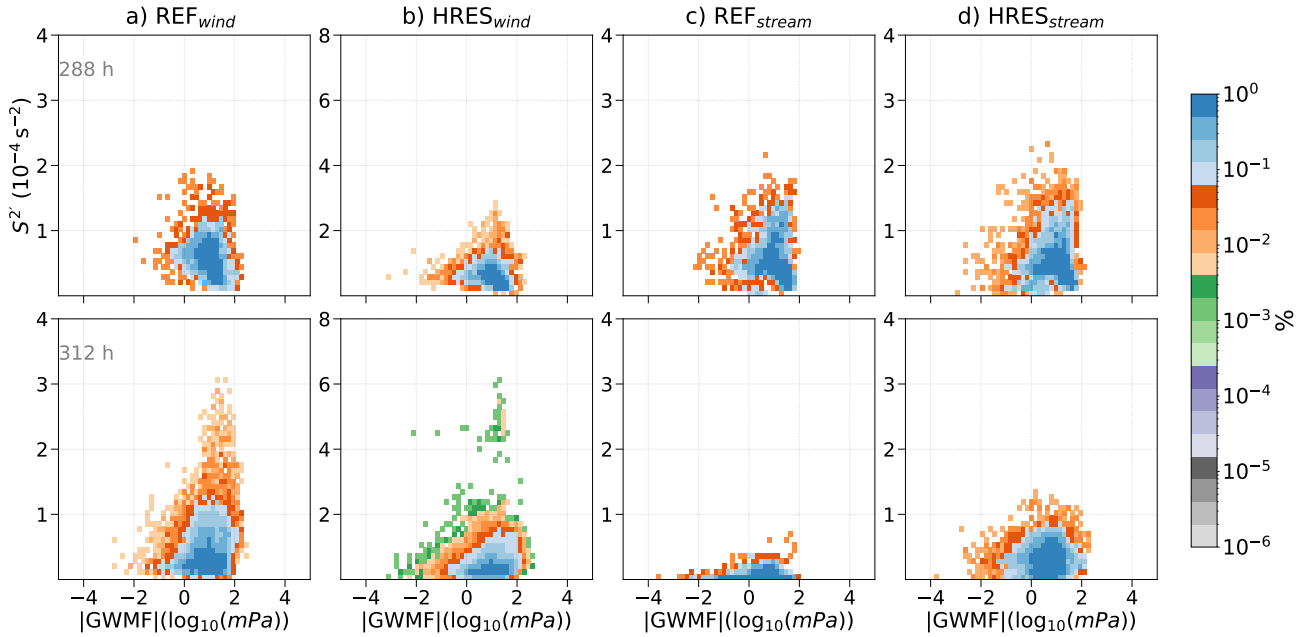


Figure 11. Relative occurrence frequency or probability density distribution of absolute momentum flux due to GWs |GWMF| - vertical shear, $S^{2'}$ on small scale, pairs in the LMS for $Ri \leq 5$ for simulations with grid spacing sensitivity. Normalized counts of PDFs distribution. Logarithmic occurrence frequency color scale.

below $1/4$ occur. The shear values reach up to ten times higher than in the dry cases. Thus, moist processes in the troposphere seem to be eminently important for the occurrence of dynamic instability in the LMS. At least to the point that moist processes substantially increase the probability of an instability to form. In contrast, the inclusion of the turbulence scheme in the model setup reduces this probability again. The case of REF_{wind} TURB still shows more occurrence of low Richardson numbers than the corresponding dry case, but TKE can also be produced. The shear, in a way, also contributes to the enhanced values of TKE and might thus explain its enhancements and vice versa. REF_{wind} CMP shows strong $S^{2'}$ values dynamically correlate with the larger N^2 , indicating strong signatures of dynamic shear instability. Shear instability occurs when the vertical wind shear is large enough to overcome the tendency of stratified flow to remain stratified, and then KHI and vortexes form. These instabilities generally resulted from strong temperature gradient and wind shear induced by GWs (Fritts and Alexander, 2003). REF_{wind} TURB CMP mirrors the behavior of REF_{wind} CMP. Noticeable here in REF_{wind} TURB Moist is the appearance of lower Ri attributed to latent heat release as discussed in the sect. 3.3. The turbulence counteracts the effects of dry dynamics, which enhance the lower stratospheric static stability (Koch et al., 2005).

Moreover, due to the tendency of turbulence to reduce the strong vertical gradients, a lower vertical shear is expected in this case. However, the TURB MOIST case shows much less potential turbulence from the small scales, even compared to its companion simulation CMP TURB. It is remarkable that in this case the N^2 - S^2 distribution differs substantially from

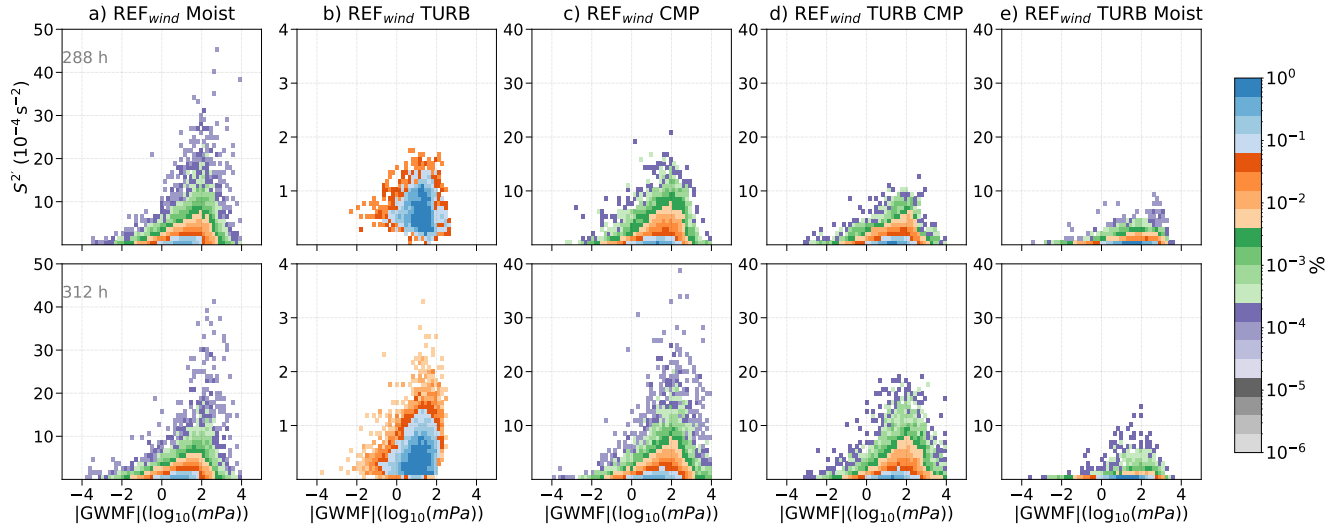


Figure 12. As in Figure 11 but for simulations with physical processes sensitivity. Normalized counts of PDFs distribution. Logarithmic occurrence frequency color scale.

the N^2 - $S^{2'}$ distribution. Thus, much of the potential turbulence in TURB Moist is evident on larger scales. To further demonstrate this, the vertical distribution of TKE is found to be enhanced by a factor of 50 in TURB Moist compared to TURB CMP and TURB. There are two sources for the generation of TKE: first, the vertical shear, and, secondly, the vertical gradient of total moisture, which can consequently lead to buoyant heat flux (Doms et al., 2011). Although the vertical shear was observed to be similar in all turbulence included cases, the subsequent buoyant heat flux in TURB Moist shows positive and negative values at the region of larger TKE values around tropopause, most probably related to the sub-synoptic waves (not shown). Due to this, $N^{2'}$ - $S^{2'}$ spectrum shows a drastic decrease in grid volumes associated with low Ri . Ultimately, there is the existence of a large overlap between enhanced shear and low Richardson number, as well as GW activity.

465

We will further explore this relation through the inclusion of the small-scale momentum flux (Figures 11 and 12). If the small scales play a major role in the shear and turbulence generation, then we expect a positive correlation between $S^{2'}$ and absolute GWMF in case of turbulence occurrence. When we filter the data of our simulations for potential turbulence, i.e., $Ri \leq 5$ in the LMS, we find a positive correlation. We interpret this as an indication that the small scales and, here in particular, the gravity waves contribute substantially to the occurrence of high shear and potential turbulence. This relation is evident in the dry simulations, also across the various sensitivity experiments (see Figure 11 for the RES and HRES experiments), as well as for the sensitivity simulations with physics (see Figure 12). Note here that the results are not strongly dependent on the wavenumber used to separate the background from the small scales.

470

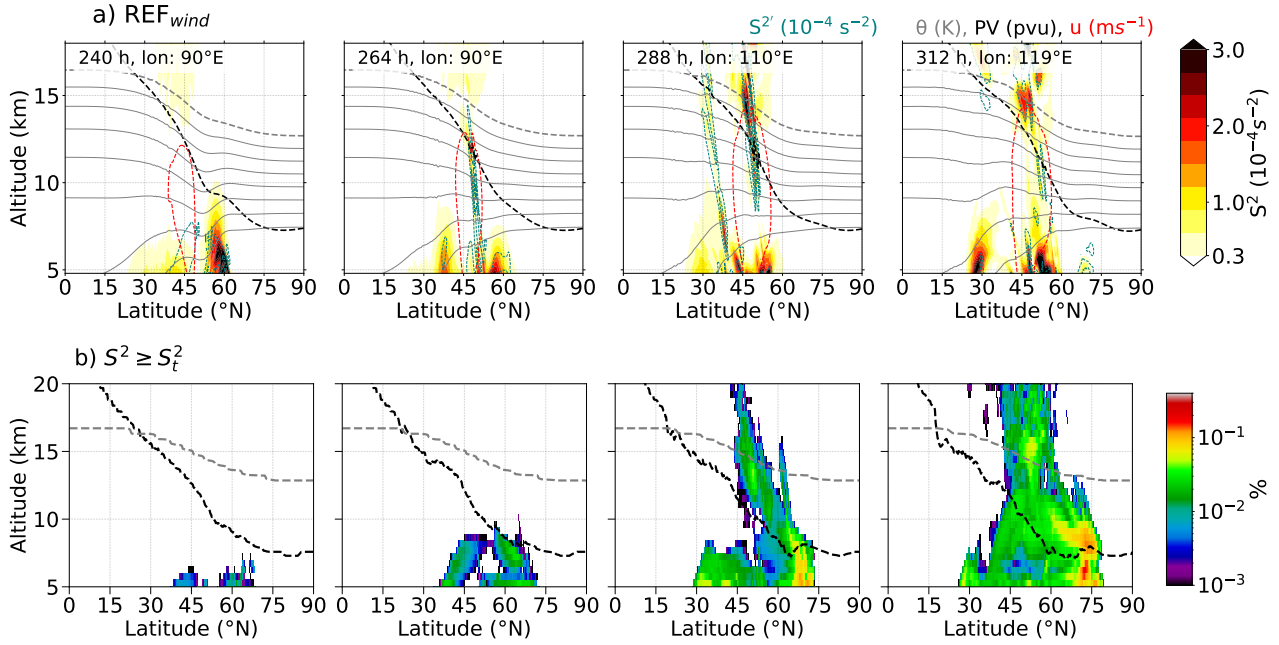


Figure 13. The temporal evolution of (a) vertical cross section of shear through the identified regions of GWs from time 240 h onward for REF_{wind} simulation with $S^{2'}$ (dashed green), potential temperature (grey), zonal wind ($30 m.s^{-1}$, red) and dynamical tropopause (black) and (b) the respective Northern hemispheric occurrence frequency distribution of grid volumes that exhibit $S^2 \geq S_t^2$. Logarithmic frequency contour, vertically binned in $dz=500$ m. The zonal mean dynamical tropopause altitude is indicated by the dashed black line and tropical tropopause (380 K isentrope) by grey dashed line.

Overall, our results strongly highlight the important role of GWs in determining potential turbulence in the LMS. Consequently, they will also play a vital role in turbulent mixing of trace species in this region and thus in the formation of the extratropical transition layer (Hoor et al., 2004; Pan et al., 2006). Since the potential turbulence occurrence is strongly linked to enhanced shear, we will now explore in more detail the role of the small-scale dynamics in the formation of the tropopause shear layer.

5 Occurrence of TSL and associated GWs

To this point, the discussion has centered on enhanced shear generation and the potential for turbulence occurrence and consequent mixing. In this section, we shift our focus to the occurrence of the tropopause shear layer (TSL) in the extratropics and its potential association with GWs in the LMS. The TSL has been defined via an exceedance of a threshold value of vertical wind shear. In Kaluza et al. (2021), the authors calculated the occurrence frequency of such a threshold exceedance in tropopause following coordinate over a ten-year data set for the Northern Hemisphere. Here, we adopt this approach for our data but do the analysis on an instantaneous time step. Our goal is to show that the occurrence

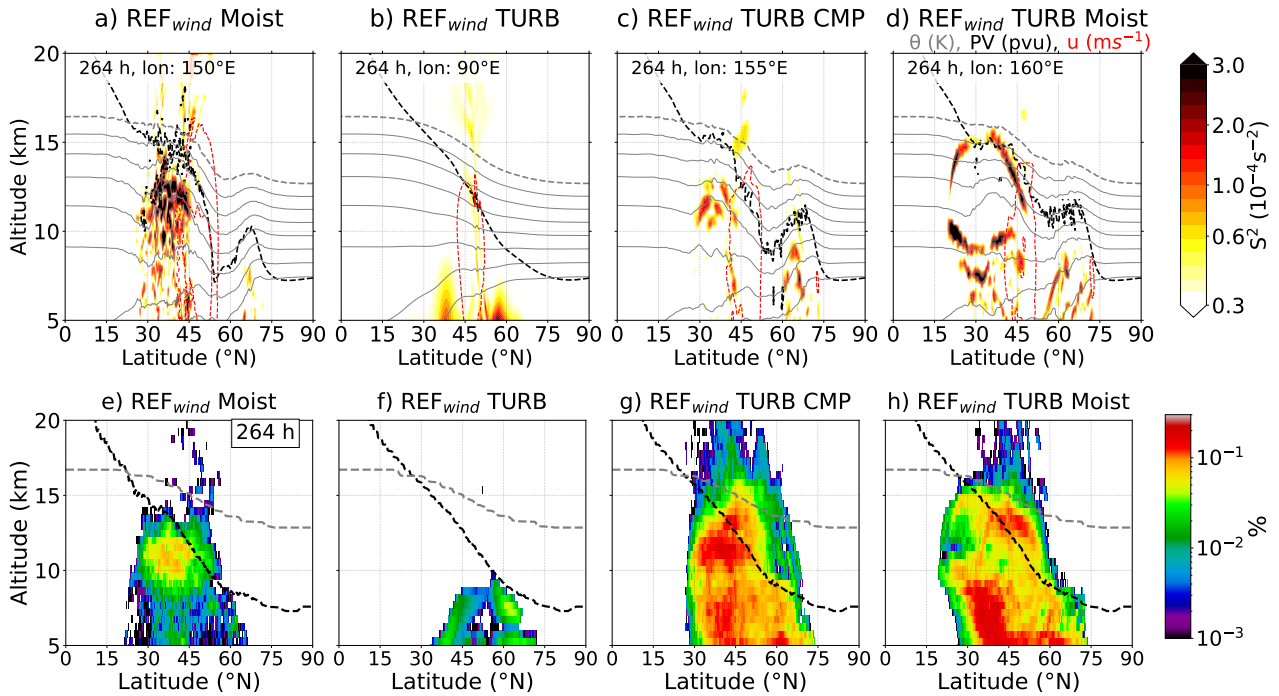


Figure 14. Vertical cross section of shear (upper panel) through the identified regions of GWs at 264 h REF_{wind} simulations with physical processes sensitivity and the respective Northern hemispheric occurrence frequency distribution of grid volumes that exhibit $S^2 \geq S_t^2$ (lower panel). Logarithmic frequency contour, vertically binned in $dz=500$ m. The zonal mean dynamical tropopause altitude is indicated by the dashed black line and tropical tropopause (380 K isentrope) by grey dashed line.

frequencies of enhanced vertical wind shear occur temporally aligned with the presence of GW in the LMS. In contrast to Kaluza et al. (2021), we start from a state with no TSL, which allows us to analyze the temporal evolution of the shear in the LMS. We follow the steps outlined in Kaluza et al. (2021) with some adaptations for our simulations.

490

The threshold value is selected based on the criterion that $S^2 \geq S_t^2$ is typically unsustainable under the average tropospheric static stability, $\overline{N^2}_{trop}$, which results in low Ri and conditions favorable for turbulence. Following this, we defined threshold value $S_t^2 = 0.3 \times 10^{-4} s^{-2}$ for dry cases and $S_t^2 = 2 \times 10^{-4} s^{-2}$ for experiments incorporating physical processes. Note, these values are much lower than the threshold defined in Kaluza et al. (2021), which is mainly rooted in the idealized setup compared to a fully comprehensive reanalysis system. For dry experiments, the chosen threshold accounts for inherently low shear occurrences and ensures the full spectrum of shear is captured. Figure 13a) demonstrates the temporal evolution of vertical cross section of shear S^2 , zonal wind u , PV and potential temperature. Notably, the region of $S^{2'}$ is strongly affected by a small-scale wave pattern related to an upward propagating GW, evident in the potential temperature and PV isolines. Meanwhile, the spatiotemporal overlap of GW signatures and $S^{2'}$, particularly after 288 h, indicates that GW is an important, if not the major, source of the enhanced values of shear occurrence in the LMS. Figure

495

500



13b) shows the temporal evolution of relative occurrence frequency counted in zonal direction for vertical wind shear S^2 on a logarithmic color scale for the northern hemisphere, with the geometric altitude as the vertical coordinate. Figure 13b) reveals regions of distinct occurrence frequency located in UTLS: one in the mid-latitudes between 40–55° N and the second one between 60–75° N above the dynamical tropopause in the extratropics. The progression of enhanced shear over time, with significant enhancement in the LMS, appears to follow the occurrence of the GW in the BLC and is tightly linked to the breaking of the synoptic scale wave. We note here that the REF_{stream} simulation exhibits a similar pattern. As discussed in section 3.4 and in the paragraph above, the growing GW trains amplify S^2 maxima and induce shear in the extra-tropics, with upward propagating GWs inducing pronounced shear in the vicinity of the tropopause and the LMS. This overlap between the pronounced shear occurrence and GW activity through the lowermost stratosphere strongly proposes that GWs are the source of enhanced shear generation in the LMS.

Furthermore, an analysis of TSL occurrence across sensitivity experiments, including grid spacing and physical forcing, also suggests that GWs play a dominant role in generating enhanced vertical shear. For the simulations with moisture and turbulence parameterization, we see a similar temporal evolution of the vertical shear in the UTLS. Major differences are related to the TURB CMP and TURB Moist showing firm $S^2 \geq S_t^2$ occurrences due to contributions from sub-synoptic features and enhanced turbulent processes. Here, the vertical shear distribution broadens with altitude, shifting toward higher values, with the peak shear predominantly concentrated in the extratropical upper troposphere (see Figure 14). This peak shear occurrence just below the tropopause, as noted by Kaluza et al. (2022), aligns with the sharp unimodal turbulence distribution. The observed colocation of shear generated due GWs and peak shear occurrence in the UT reveals the substantial contribution from small-scale features, particularly GWs, along with moist tropospheric dynamics. Overall, these findings support the hypothesis that GWs contribute to enhanced shear occurrence, that is, tropopause wind shear layer in the extratropical LMS. Broadly speaking, our results suggest that GWs play a pivotal role in shaping TSL dynamics and consequently contribute to the formation and maintenance of ExTL.

6 Summary and conclusion

In this study, we investigate the role of GWs in generating vertical wind shear and potential turbulence and their contribution to the formation of regions of enhanced vertical shear in the extratropical lowermost stratosphere. Using idealized baroclinic life cycle experiments with ICON, we examine the impact of model grid spacing and non-conservative processes including moisture, cloud microphysics and turbulence, on the GW emergence and the generation of shear. Our findings emphasize that GWs, driven by baroclinic wave dynamics, are pivotal in enhancing vertical wind shear and promoting turbulence in this region. This highlights several key implications of GWs on vertical shear generation:

1. GWs appearance and associated shear are highly dependent on the model grid spacing. A distinct change in the emergence of GW occurs when a horizontal model grid spacing finer than 20 km is applied. More so, and also less important in our case, we see more GW signs with shorter wavelengths for the vertical grid spacing currently



used in NWP models, i.e., $dz \sim 300$ m, compared to simulations with $dz \sim 1$ km. This highlights the necessity to properly simulate GWs and to capture small-scale processes considering suitable higher spatial resolution. Besides this, using the DCMIP initial states in both forms of wind and stream perturbations gives similar evolution of the GW life cycles and leads to same conclusion in terms of role of GWs in shear and potential turbulence generation in the UTLS.

2. Physical processes, such as moisture, significantly influence the extent and occurrence of GW, and thus, shear and turbulence occurrence in the LMS. Moist simulations revealed that latent heat release in the troposphere enhances GW near the tropopause, leading to substantial shear enhancement in the lower stratosphere.

These results are quite robust for different model settings in terms of spatial and temporal resolution and physics parameterizations. This gives further confidence that GW breaking are of relevance for the overall occurrence of enhanced shear in the lowermost stratosphere.

3. Further indication of the role of GWs for shear and turbulence generation in the LMS is found through a spatio-temporal correlation between small-scale momentum flux, enhanced shear and low Richardson numbers. This correlation is independent of our model configuration and is found in dry, moist and turbulent experiments of baroclinic waves.

4. The occurrence frequency of strong vertical shear near the tropopause peaks at extratropical LMS, and correlates with GW activity, suggesting that GW amplify shear maxima and lead to shear enhancement near the tropopause. TSL analysis highlights that upward-propagating GWs are a major contributor to enhanced vertical shear in the LMS, particularly associated with the breaking of synoptic scale wave.

Regarding 2, the sudden shear enhancement in moist experiments is due to the latent heating release and its effect on the overall evolution of the baroclinic wave. The faster evolution of the baroclinic wave, along with stronger upward motions, substantially affects the presence of GWs in the LMS in terms of number, magnitude, and growth rate. This, in turn, leads to much higher shear values and lower Richardson numbers, i.e., more regions prone to become dynamically unstable. Ultimately, this highlights the role of tropospheric dynamics for the potential mixing of air masses due to small-scale dynamics in the LMS.

Further investigation into the relationship between GWs and TSL is warranted, as both appear consistently in climatological data based on zonal and temporal tropopause averages (Birner et al., 2002; Zhang et al., 2019). The enhanced shear associated with GWs substantially is a key for the emergence of the shear layer above the extratropical tropopause and, thus, a crucial feature in the formation and maintenance of the extratropical transition layer, a region identifiable through chemical tracer observations (e.g., Hoor et al., 2004; Pan et al., 2006; Birner, 2006). It is found that the GWs originating from baroclinic waves are pivotal in shaping the structure and dynamics of the extratropical LMS. The observed GW momentum flux and enhanced zonal shear correlation supports the dominant role of GWs in TSL development, highlighting their potential influence on STE, turbulent mixing and ultimately the distribution of chemical species in



the tropopause region.

570 Despite the valuable insights gained in this study, there are some limitations that should be acknowledged. First, the use
of an idealized setup with short simulation times and specific initial states does not account for seasonal and inter-annual
variations. Additionally, key processes such as convection were neglected and the representation of GW spectrum may be
insufficient to fully capture the complexity of small-scale GW dynamics. These limitations suggest that further investiga-
575 tion is needed to comprehensively understand the role of GWs in shear enhancement and turbulent mixing in the LMS. To
address these gaps, future work could build upon this study by simulating real-case scenarios using more comprehensive
model setups, including processes like convection and improved GW parameterizations. Conducting longer simulations
would allow for a better understanding of the processes driving the TSL and capturing seasonal and inter-annual varia-
tions. Moreover, generating a climatological dataset of small-scale GWs in the UTLS, validated by long-term observational
data, would provide valuable guidance on the sources contributing to the TSL and their broader atmospheric implications.
580 On the other hand, validation of these results using orographic and non-orographic GW parameterizations might help to
thoroughly explain the role of GWs in STE and mixing in the LMS.

Overall, our findings highlight the crucial role of GWs in enhancement of vertical shear and facilitating potential turbulent
mixing in the extratropical LMS, ultimately contributing to the formation of the extratropical transition layer. These results
585 underscore the importance of accounting for GWs in the prediction of clear air turbulence, as their influence on unforeseen
turbulence events cannot be neglected. This opens door for further exploration of how sub-grid-scale GWs influence
vertical shear and transport processes in the UTLS, particularly their role in the tropopause shear layer and stratosphere-
troposphere exchange.

Code and data availability. The ICON source code is provided under an institutional license granted by the German Weather Service
590 (DWD). Further details can be found at <https://code.mpimet.mpg.de/projects/iconpublic> (DWD and MPI, 2015). The model output from
the ICON simulations can be obtained from the authors upon request. The processed data, python scripts used for calculations and
plot generation are made publicly available at <https://doi.org/10.5281/zenodo.14334535>.

Author contributions. DK conceptualized the core research questions and goals. MU conducted the data analysis, wrote the post-
processing code, and drafted the manuscript. MU and DK jointly contributed to the interpretation of the results and the final editing of
595 the manuscript.

Competing interests. The authors declare that they have no competing interests.



Acknowledgements. This work was funded by the Deutsche Forschungsgemeinschaft (DFG, German Research Foundation) – TRR 301 – Project-ID 428312742: “The tropopause region in a changing atmosphere, <https://tpchange.de/>” sub-project B06. The authors gratefully acknowledge the computing time provided on the supercomputer MOGON II at Johannes Gutenberg University Mainz (hpc. uni-mainz.de). We further thank Ulrich Achatz and Juerg Schmidli from Goethe-Universität Frankfurt for their valuable comments and feedback on this work. We greatly appreciate the useful discussion input by Peter Hoor. Special thanks are due to Thorsten Kaluza of University of Reading, UK, for insightful discussion and technical assistance at an early stage of this work.



References

- Achatz, U., Alexander, M. J., Becker, E., Chun, H. Y., Dörnbrack, A., Holt, L., Plougonven, R., Polichtchouk, I., Sato, K., Sheshadri, A., Stephan, C. C., Van Niekerk, A., and Wright, C. J.: Atmospheric Gravity Waves: Processes and Parameterization, *Journal of the Atmospheric Sciences*, 81, 237–262, <https://doi.org/10.1175/JAS-D-23-0210.1>, 2024.
- Alexander, M. J., Geller, M., McLandress, C., Polavarapu, S., Preusse, P., Sassi, F., Sato, K., Eckermann, S., Ern, M., Hertzog, A., Kawatani, Y., Pulido, M., Shaw, T. A., Sigmond, M., Vincent, R., and Watanabe, S.: Recent developments in gravity-wave effects in climatemodels and the global distribution of gravity-wavemomentum flux from observations and models, *Quarterly Journal of the Royal Meteorological Society*, 136, 1103–1124, <https://doi.org/10.1002/qj.637>, 2010.
- Andrews, D. G., Taylor, F. W., and McIntyre, M. E.: The Influence of Atmospheric Waves on the General Circulation of the Middle Atmosphere [and Discussion], *Philosophical Transactions of the Royal Society of London. Series A, Mathematical and Physical Sciences*, 323, 693–705, <http://www.jstor.org/stable/38143>, 1987.
- Birner, T.: Fine-scale structure of the extratropical tropopause region, *Journal of Geophysical Research Atmospheres*, 111, 1–14, <https://doi.org/10.1029/2005JD006301>, 2006.
- Birner, T., Dörnbrack, A., and Schumann, U.: How sharp is the tropopause at midlatitudes?, *Geophysical Research Letters*, 29, 1–4, <https://doi.org/10.1029/2002GL015142>, 2002.
- Doms, G., Förstner, J., Heise, E., Herzog, H.-J., Mironov, D., Raschendorfer, M., Reinhardt, T., Ritter, B., Schrodin, R., Schulz, J.-P., and Vogel, G.: Consortium for Small-Scale Modelling A Description of the Nonhydrostatic Regional COSMO Model Part II : Physical Parameterization, *Www.Cosmo-Model.Org*, p. 152, 2011.
- Durran, D. R.: Pseudomomentum Diagnostics for Two-Dimensional Stratified Compressible Flow, *Journal of Atmospheric Sciences*, 52, 3997 – 4009, [https://doi.org/10.1175/1520-0469\(1995\)052<3997:PDFTDS>2.0.CO;2](https://doi.org/10.1175/1520-0469(1995)052<3997:PDFTDS>2.0.CO;2), 1995.
- Erlar, A. R. and Wirth, V.: The static stability of the tropopause region in adiabatic baroclinic life cycle experiments, *Journal of the Atmospheric Sciences*, 68, 1178–1193, <https://doi.org/10.1175/2010JAS3694.1>, 2011.
- Fritts, D. C. and Alexander, M. J.: Gravity wave dynamics and effects in the middle atmosphere, *Reviews of Geophysics*, 41, 1–64, <https://doi.org/10.1029/2001RG000106>, 2003.
- Hegglin, M. I., Boone, C. D., Manney, G. L., and Walker, K. A.: A global view of the extratropical tropopause transition layer from Atmospheric Chemistry Experiment Fourier Transform Spectrometer O₃, H₂O, and CO, *Journal of Geophysical Research Atmospheres*, 114, 1–18, <https://doi.org/10.1029/2008JD009984>, 2009.
- Hodges Jr., R. R.: Generation of turbulence in the upper atmosphere by internal gravity waves, *Journal of Geophysical Research* (1896-1977), 72, 3455–3458, <https://doi.org/https://doi.org/10.1029/JZ072i013p03455>, 1967.
- Hoerling, M. P., Schaack, T. K., and Lenzen, A. J.: Global Objective Tropopause Analysis, *Monthly Weather Review*, 119, 1816–1831, [https://doi.org/10.1175/1520-0493\(1991\)119<1816:gota>2.0.co;2](https://doi.org/10.1175/1520-0493(1991)119<1816:gota>2.0.co;2), 1991.
- Holton, J. R., Haynes, P. H., McIntyre, M. E., Douglass, A. R., Rood, R. B., and Pfister, L.: Stratosphere-troposphere exchange, *Reviews of Geophysics*, 33, 403–439, <https://doi.org/10.1029/95RG02097>, 1995.
- Hoor, P., Gurk, C., Brunner, D., Hegglin, M. I., Wernli, H., and Fischer, H.: Seasonality and extent of extratropical TST derived from in-situ CO measurements during SPURT, *Atmospheric Chemistry and Physics*, 4, 1427–1442, <https://doi.org/10.5194/acp-4-1427-2004>, 2004.



- Hoskins, B. J., McIntyre, M. E., and Robertson, A. W.: On the use and significance of isentropic potential vorticity maps, *The Quarterly Journal of the Royal Meteorological Society*, 111, 877–946, <https://doi.org/10.1002/qj.49711146602>, 1985.
- Jablonowski, C. and Williamson, D. L.: A baroclinic instability test case for atmospheric model dynamical cores, *Quarterly Journal of the Royal Meteorological Society*, 132, 2943–2975, <https://doi.org/10.1256/qj.06.12>, 2006.
- Kaluza, T., Kunkel, D., and Hoor, P.: Composite analysis of the tropopause inversion layer in extratropical baroclinic waves, *Atmospheric Chemistry and Physics*, 19, 6621–6636, <https://doi.org/10.5194/acp-19-6621-2019>, 2019.
- 645 Kaluza, T., Kunkel, D., and Hoor, P.: On the occurrence of strong vertical wind shear in the tropopause region: a 10-year ERA5 northern hemispheric study, *Weather and Climate Dynamics*, 2, 631–651, <https://doi.org/10.5194/wcd-2-631-2021>, 2021.
- Kaluza, T., Kunkel, D., and Hoor, P.: Analysis of Turbulence Reports and ERA5 Turbulence Diagnostics in a Tropopause-Based Vertical Framework, 49, e2022GL100 036, <https://doi.org/10.1029/2022GL100036>, 2022.
- Koch, S. E., Jamison, B. D., Lu, C., Smith, T. L., Tollerud, E. I., Girz, C., Wang, N., Lane, T. P., Shapiro, M. A., Parrish, D. D., and
 650 Cooper, O. R.: Turbulence and Gravity Waves within an Upper-Level Front, *Journal of the Atmospheric Sciences*, 62, 3885–3908, <https://doi.org/10.1175/jas3574.1>, 2005.
- Kunkel, D., Hoor, P., and Wirth, V.: Can inertia-gravity waves persistently alter the tropopause inversion layer?, *Geophysical Research Letters*, 41, 7822–7829, <https://doi.org/10.1002/2014GL061970>, 2014.
- Kunkel, D., Hoor, P., and Wirth, V.: The tropopause inversion layer in baroclinic life-cycle experiments: The role of diabatic processes,
 655 *Atmospheric Chemistry and Physics*, 16, 541–560, <https://doi.org/10.5194/acp-16-541-2016>, 2016.
- Kunkel, D., Hoor, P., Kaluza, T., Ungermann, J., Kluschat, B., Giez, A., Lachnitt, H. C., Kaufmann, M., and Riese, M.: Evidence of small-scale quasi-isentropic mixing in ridges of extratropical baroclinic waves, *Atmospheric Chemistry and Physics*, 19, 12 607–12 630, <https://doi.org/10.5194/acp-19-12607-2019>, 2019.
- Lachnitt, H. C., Hoor, P., Kunkel, D., Bramberger, M., Dörnbrack, A., Müller, S., Reutter, P., Giez, A., Kaluza, T., and Rapp, M.:
 660 Gravity-wave-induced cross-isentropic mixing: A DEEPWAVE case study, *Atmospheric Chemistry and Physics*, 23, 355–373, <https://doi.org/10.5194/acp-23-355-2023>, 2023.
- Lane, T. P. and Sharman, R. D.: Gravity wave breaking, secondary wave generation, and mixing above deep convection in a three-dimensional cloud model, *Geophysical Research Letters*, 33, <https://doi.org/10.1029/2006gl027988>, 2006.
- Lane, T. P., Reeder, M. J., and Clark, T. L.: Numerical Modeling of Gravity Wave Generation by Deep Tropical Convection, *Journal of the Atmospheric Sciences*, 58, 1249–1274, [https://doi.org/10.1175/1520-0469\(2001\)058<1249:nmogwg>2.0.co;2](https://doi.org/10.1175/1520-0469(2001)058<1249:nmogwg>2.0.co;2), 2001.
- 665 Lane, T. P., Doyle, J. D., Plougonven, R., Shapiro, M. A., and Sharman, R. D.: Observations and Numerical Simulations of Inertia–Gravity Waves and Shearing Instabilities in the Vicinity of a Jet Stream, *Journal of the Atmospheric Sciences*, 61, 2692–2706, <https://doi.org/10.1175/jas3305.1>, 2004.
- Luderer, G., Trentmann, J., Hungershofer, K., Herzog, M., Fromm, M., and Andreae, M. O.: Small-scale mixing processes enhancing
 670 troposphere-to-stratosphere transport by pyro-cumulonimbus storms, <https://doi.org/10.5194/acpd-7-10371-2007>, 2007.
- O’sullivan, D. and Dunkerton, T. J.: Generation of Inertia–Gravity Waves in a Simulated Life Cycle of Baroclinic Instability, *Journal of Atmospheric Sciences*, 52, 3695 – 3716, [https://doi.org/10.1175/1520-0469\(1995\)052<3695:GOIWIA>2.0.CO;2](https://doi.org/10.1175/1520-0469(1995)052<3695:GOIWIA>2.0.CO;2), 1995.
- Pan, L. L., Konopka, P., and Browell, E. V.: Observations and model simulations of mixing near the extratropical tropopause, *Journal of Geophysical Research Atmospheres*, 111, 1–15, <https://doi.org/10.1029/2005JD006480>, 2006.
- 675 Plougonven, R. and Snyder, C.: Gravity waves excited by jets: Propagation versus generation, *Geophysical Research Letters*, 32, 1–4, <https://doi.org/10.1029/2005GL023730>, 2005.



- Plougonven, R. and Zhang, F.: INTERNAL GRAVITY WAVES FROM, <https://doi.org/10.1002/2012RG000419.1>.INTRODUCTION, 2013.
- Plougonven, R. and Zhang, F.: Internal gravity waves from atmospheric jets and fronts, *Reviews of Geophysics*, 52, 33–76, <https://doi.org/10.1002/2012RG000419>, 2014.
- Plougonven, R., Teitelbaum, H., and Zeitlin, V.: Inertia gravity wave generation by the tropospheric midlatitude jet as given by the Fronts and Atlantic Storm-Track Experiment radio soundings, *Journal of Geophysical Research: Atmospheres*, 108, <https://doi.org/10.1029/2003jd003535>, 2003.
- Prill, F., Reinert, D., Rieger, D., and Zängl, G.: ICON tutorial 2020, <https://doi.org/10.5676/DWD>, 2020.
- Raschendorfer, M.: The new turbulence parameterization of LM, *COSMO Newsletter No. 1*, pp. 89–97, 2001.
- Seifert, A.: On the parameterization of evaporation of raindrops as simulated by a one-dimensional rainshaft model, *Journal of the Atmospheric Sciences*, 65, 3608–3619, <https://doi.org/10.1175/2008JAS2586.1>, 2008.
- Shapiro, M. A.: Further Evidence of the Mesoscale and Turbulent Structure of Upper Level Jet Stream–Frontal Zone Systems, *Monthly Weather Review*, 106, 1100–1111, [https://doi.org/10.1175/1520-0493\(1978\)106<1100:feotma>2.0.co;2](https://doi.org/10.1175/1520-0493(1978)106<1100:feotma>2.0.co;2), 1978.
- Shepherd, T. G.: Transport in the Middle Atmosphere, *Journal of the Meteorological Society of Japan. Ser. II*, 85B, 165–191, <https://doi.org/10.2151/jmsj.85B.165>, 2007.
- Spreitzer, E., Attinger, R., Boettcher, M., Forbes, R., Wernli, H., and Joos, H.: Modification of potential vorticity near the tropopause by nonconservative processes in the ECMWF model, *Journal of the Atmospheric Sciences*, 76, 1709–1726, <https://doi.org/10.1175/JAS-D-18-0295.1>, 2019.
- Thorncroft, C. D., Hoskins, B. J., and McIntyre, M. E.: Two paradigms of baroclinic-wave life-cycle behaviour, *Quarterly Journal of the Royal Meteorological Society*, 119, 17–55, <https://doi.org/10.1002/qj.49711950903>, 1993.
- Trier, S. B., Sharman, R. D., Muñoz-Esparza, D., and Lane, T. P.: Environment and mechanisms of severe turbulence in a midlatitude cyclone, *Journal of the Atmospheric Sciences*, 77, 3869–3889, <https://doi.org/10.1175/JAS-D-20-0095.1>, 2020.
- Ullrich, P. A., Melvin, T., Jablonowski, C., and Staniforth, A.: A proposed baroclinic wave test case for deep- and shallow-atmosphere dynamical cores, *Quarterly Journal of the Royal Meteorological Society*, 140, 1590–1602, <https://doi.org/10.1002/qj.2241>, 2014.
- Ullrich, P. A., Jablonowski, C., Kent, J., Lauritzen, P. H., Nair, R., Reed, K. A., Zarzycki, C. M., Hall, D. M., Dazlich, D., Heikes, R., Konor, C., Randall, D., Dubos, T., Meurdesoif, Y., Chen, X., Harris, L., Kühnlein, C., Lee, V., Qaddouri, A., Girard, C., Giorgetta, M., Reinert, D., Klemp, J., Park, S. H., Skamarock, W., Miura, H., Ohno, T., Yoshida, R., Walko, R., Reinecke, A., and Viner, K.: DCMIP2016: A review of non-hydrostatic dynamical core design and intercomparison of participating models, *Geoscientific Model Development*, 10, 4477–4509, <https://doi.org/10.5194/gmd-10-4477-2017>, 2017.
- Wang, S. and Zhang, F.: Sensitivity of Mesoscale Gravity Waves to the Baroclinicity of Jet-Front Systems, *Monthly Weather Review*, 135, 670–688, <https://doi.org/10.1175/mwr3314.1>, 2007.
- Wei, J. and Zhang, F.: Mesoscale gravity waves in moist baroclinic jet-front systems, *Journal of the Atmospheric Sciences*, 71, 929–952, <https://doi.org/10.1175/JAS-D-13-0171.1>, 2014.
- Weyland, F., Hoor, P., Kunkel, D., Birner, T., Plöger, F., and Turhal, K.: Long-term changes in the thermodynamic structure of the lowermost stratosphere inferred from ERA5 reanalysis data, pp. 1–26, 2024.
- Whiteway, J. A., Klaassen, G. P., Bradshaw, N. G., and Hacker, J.: Transition to turbulence in shear above the tropopause, *Geophysical Research Letters*, 31, 2–5, <https://doi.org/10.1029/2003GL018509>, 2004.



- Zängl, G., Reinert, D., Rípodas, P., and Baldauf, M.: The ICON (ICOsahedral Non-hydrostatic) modelling framework of DWD and
 715 MPI-M: Description of the non-hydrostatic dynamical core, *Quarterly Journal of the Royal Meteorological Society*, 141, 563–579,
<https://doi.org/10.1002/qj.2378>, 2015.
- Zhang, F.: Generation of mesoscale gravity waves in upper-tropospheric jet-front systems, *Journal of the Atmospheric Sciences*, 61,
 440–457, [https://doi.org/10.1175/1520-0469\(2004\)061<0440:GOMGWI>2.0.CO;2](https://doi.org/10.1175/1520-0469(2004)061<0440:GOMGWI>2.0.CO;2), 2004.
- Zhang, Y., Zhang, S., Huang, C., Huang, K., Gong, Y., and Gan, Q.: The interaction between the tropopause inversion layer and the
 720 inertial gravity wave activities revealed by radiosonde observations at a midlatitude station, *Journal of Geophysical Research*, 120,
 8099–8111, <https://doi.org/10.1002/2015JD023115>, 2015.
- Zhang, Y., Zhang, S., Huang, C., Huang, K., and Gong, Y.: The Tropopause Inversion Layer Interaction With the Iner-
 tial Gravity Wave Activities and Its Latitudinal Variability, *Journal of Geophysical Research: Atmospheres*, 124, 7512–7522,
<https://doi.org/10.1029/2019JD030309>, 2019.
- 725 Zülicke, C. and Peters, D.: Simulation of inertia-gravity waves in a poleward-breaking Rossby wave, *Journal of the Atmospheric Sci-*
ences, 63, 3253–3276, <https://doi.org/10.1175/JAS3805.1>, 2006.